
Extended Modeling and Control of Quadrotors using System Identification

Thesis Report

A. Nair (1036569)

Coach: dr. ir. A.A.J. Lefeber (TU/e)

Supervisor: prof. dr. H. Nijmeijer (TU/e)

Department of Mechanical Engineering
Dynamics and Control (D&C) group
Eindhoven University of Technology

Eindhoven, April 15, 2019

Summary

Autonomous drones are required to follow a pre-defined trajectory without any need of manual operation. For many applications with cooperative quadrotors, fast-maneuvering with good tracking capabilities is an important requirement to avoid collisions. A previously designed controller for a quadrotor UAV is capable of tracking slow varying trajectories with good accuracy. However, for aggressive maneuvering the controller cannot simultaneously reject the disturbance dynamics and accurately track the given trajectory. The main objective of this thesis is to re-design the tracking controller with the extended dynamic model obtained using identification methods. Aerodynamic effects have the most dominant role in these disturbances and first principles models of the aerodynamic forces and moments are computationally expensive. Data-driven modeling is a more economic approach which is used to identify the disturbances at several operating regions of the drone. In this project, grey-box models are defined to capture the disturbance dynamics which are partially based on prior knowledge of quadrotor aerodynamics. Experimental flight data are used to select the most appropriate model structure and also estimate the parameters of the chosen model. The validated model for disturbance forces and moments are updated to the cascaded controller such that almost-global uniform asymptotic stability is proved using known stability results. The identified extended model has been implemented in a simulation environment and compared with experimental results. The position results are compared for the case of a three dimensional circular trajectory and a vertical eight figure trajectory. Simulation results of the extended model without the identified moment models show good match with the actual quadrotor position measurements. The identified moment models generated undesired results which is believed to be caused by poor parameter estimates. Therefore, the implementation of the redesigned controller in the simulation environment does not include the compensation for disturbance moments. Considering the quadrotor airspeed, disturbance moments have very little influence on the tracking performance. Simulation of the redesigned controller for the extended model shows improved position tracking performance. The exclusion of the disturbance force compensation term from the controller results in a large deviation of the quadrotor position from the given trajectory.

Contents

| | |
|--|-----------|
| Summary | i |
| Nomenclature | iv |
| 1 Introduction | 1 |
| 1.1 Background | 1 |
| 1.2 Literature Review | 2 |
| 1.3 Motivation and Objectives | 4 |
| 1.4 Problem Formulation | 4 |
| 1.5 Thesis Outline | 6 |
| 2 Data Acquisition and Processing | 7 |
| 2.1 Attitude Observer | 7 |
| 2.2 Velocity Estimation | 9 |
| 2.3 Rotor Speed Estimation | 10 |
| 2.4 Extraction of Aerodynamic Forces and Moments | 11 |
| 2.5 Concluding Remarks | 11 |
| 3 Identification of Aerodynamic Models | 13 |
| 3.1 Model Selection | 14 |
| 3.2 Thrust Force Model | 16 |
| 3.3 Drag Force Model | 22 |
| 3.4 Roll and Pitch Moment Model | 28 |
| 3.5 Yaw Moment Model | 32 |
| 3.6 Comments on Identified Models | 34 |
| 3.7 Concluding Remarks | 36 |
| 4 Controller Re-design | 38 |
| 4.1 Preliminaries | 39 |
| 4.2 Problem Formulation | 41 |
| 4.3 Position Control Re-design | 42 |
| 4.4 Attitude Control Re-design | 44 |
| 4.5 Cascade Analysis | 45 |
| 4.6 Concluding Remarks | 46 |
| 5 Simulation Study | 48 |
| 5.1 Validation of Extended Model | 48 |
| 5.2 Re-designed Controller Simulation | 52 |

| | | |
|----------|--|-----------|
| 5.3 | Concluding Remarks | 56 |
| 6 | Conclusions and Recommendations | 57 |
| 6.1 | Conclusions | 57 |
| 6.2 | Recommendations | 58 |
| | Bibliography | 60 |
| A | Attitude Observer Simulation | 64 |
| B | Differentiation Filter | 66 |
| C | Hovering Thrust model | 67 |
| D | RLS Algorithm | 68 |
| E | Further Extended:Yaw Moment Model | 69 |

Nomenclature

List of Symbols

| | |
|----------------------|---|
| \mathbb{R}^n | n -dimensional Euclidean space |
| $\mathcal{SO}(n)$ | The n -dimensional Special Orthogonal group |
| \mathcal{B} | Right-handed orthonormal body-fixed coordinate frame |
| \mathcal{I} | Right-handed orthonormal inertial frame of reference |
| \mathcal{R} | Right-handed orthonormal tracking reference coordinate frame |
| R | Rotation matrix which transforms \mathcal{B} to \mathcal{I} |
| R_r | Rotation matrix which transforms \mathcal{R} to \mathcal{I} |
| $S(a)$ | Skew-symmetric matrix applied on vector a |
| ρ, ρ_r | Position of the origin of \mathcal{B} and \mathcal{R} respectively, relative to the center of \mathcal{I} |
| ν, ν_r | Body-fixed velocities, expressed with respect to \mathcal{B} and \mathcal{R} respectively |
| ϕ, θ, ψ | Roll, pitch and yaw angles |
| ω, ω_r | Angular velocities, expressed with respect to \mathcal{B} and \mathcal{R} respectively |
| f, τ | Quadrotor thrust and torque inputs |
| Ω_i | Rotation speed of the i^{th} rotor |
| F_{aero} | Aerodynamic force vector $[F_{a,x} \ F_{a,y} \ F_{a,z}]^T$ with respect to \mathcal{B} |
| M_{aero} | Aerodynamic moment vector $[M_{a,x} \ M_{a,y} \ M_{a,z}]^T$ with respect to \mathcal{B} |
| M_d | Disturbance moment vector $[M_{gyro,x}, M_{gyro,y}, M_{rot,z}]^T$ with respect to \mathcal{B} |
| \mathcal{E} | Estimator frame of reference |
| \hat{R} | Estimate of the body-fixed rotation matrix R which transforms \mathcal{E} to \mathcal{I} |
| ω^y | Raw gyroscope measurements in \mathcal{B} |
| a^y | Raw accelerometer measurements in \mathcal{B} |

| | |
|---|---|
| m^y | Raw magnetometer measurements in \mathcal{B} |
| v_a, v_m | normalized accelerometer and magnetometer measurements (unit vectors) |
| F_{aero}, \hat{F}_{aero} | Aerodynamic force measurement and identified model. |
| M_{aero}, \hat{M}_{aero} | Aerodynamic moment measurement and identified model. |
| M_d, \hat{M}_d | Disturbance moment measurement and identified model. |
| y | Model output. |
| ϵ | Model residue |
| Θ | Free parameters of the model set |
| $\theta, \hat{\theta}$ | Free parameters of the selected model and its estimation |
| $\nu_i, \nu_{in,i}$ | Local rotor velocity and induced velocity of rotor i . |
| V_i, V | Resultant speed of rotor i and quadrotor airspeed. |
| \hat{T}, \hat{F}_{hov} | Thrust and hovering model in z -direction. |
| α, β | Angle of attack and side slip angle. |
| $\hat{F}_{r,aero}, \hat{M}_{r,aero}, \hat{M}_{r,d}$ | Identified disturbance models with respect to reference frame \mathcal{R} . |
| f_r, τ_r | Thrust and torque inputs in \mathcal{R} . |
| $\sigma(e)$ | Saturation vector-function defined for vector e |
| t, t_0, T_s | Time, initial time and sampling time |
| ρ_e, ν_e | Position and velocity tracking errors, expressed with respect to \mathcal{R} |
| k_ρ, k_ν | Position control gains |
| \mathcal{D} | Right-handed orthonormal desired direction frame |
| f_d, R_d | Desired thrust vector and desired rotation matrix which transforms \mathcal{D} to \mathcal{R} |
| R_e, ω_e | Attitude and angular velocity tracking error expressed in \mathcal{B} |
| K_R, K_ω | Attitude control gains |

Acronyms

| | |
|-----|-------------------------|
| UAV | Unmanned Aerial Vehicle |
| NWU | North-West-Up |

| | |
|----------------|---|
| IMU | Inertial Measurement Unit |
| LAR | Least Angle Regression |
| LASSO | Least Absolute Shrinkage and Selection Operator |
| BIC | Bayesian Information Criterion |
| NMSE | Normalized Mean Square error |
| UGAS (or UGES) | Uniformly Globally (or Exponentially) Asymptotically Stable |
| UaGAS | Uniformly almost Globally Asymptotically Stable |

Chapter 1

Introduction

1.1 Background

The fascination with unmanned aerial vehicles (UAVs) is witnessed in the past years from its applications emerging in several fields. With the rapid advancement in UAV technology, the potential uses are constantly recognized by various sectors for the purposes of package delivery, cinematography, reconnaissance, farming, rescue missions and many more. The earliest known uses of UAVs go back to military operations, but now multirotor vehicles are integrated into everyday applications of the civilian world. In the field of agriculture, they are used for monitoring crop growth and also for spraying water and pesticides [1]. Film industry implements multirotor drones to capture hard-to-reach angles and dynamic action scenes due to its freedom of motion [2, 3]. Companies like Google, Amazon, UPS, and DHL have firmly invested in the idea of package delivery by UAVs instead of trucks. Such industries are drawn by the less energy consumption and reduced environmental impacts of small and compact drones [4, 5].

In disaster-affected regions, UAVs are utilized for transporting the emergency commodities, locating trapped victims and also for providing directions for safe evacuations [6]. Operations like this usually require multiple drones to fly in formation and maintain cooperation with each other to immediately scan and carry out the necessary actions [7].

The recent improvements in batteries, processors and several other components of drones have indeed contributed to improving the autonomous applications, but there are still many challenges involved in enhancing its flight capabilities. For instance, for autonomous flight motions in outdoor environments, UAVs should be capable of flying in changing wind conditions and other harsh environments. An example requiring such features is the application of autonomous drones for studying volcanoes and hurricanes, where gathering important real-time data can become very difficult. NOAA is a known scientific agency which has been using UAVs named Coyote and Global Hawk to collect data for building hurricane forecasting models [8]. Maneuvering in such conditions requires design and implementation of controllers which recognize the ambient conditions and also perform the necessary flight operations.

The design of appropriate tracking control laws for a UAV system possessing highly nonlinear and strongly intertwined dynamics with an unstable and under-actuated nature is already very challenging. In addition, the controllers are needed to take into consideration the complex aerodynamics in different air flow conditions. This demands for deriving mathematical models which describe the

behaviour of the rigid body dynamics of the quadrotor and also the disturbances acting on it in most environments. The derived models should also not undermine the processing capabilities of low-cost drones in order to enable high-speed motions. This thesis aims to determine and model the significant external disturbances for improving the tracking performance of a quadrotor UAV.

1.2 Literature Review

The aerodynamic modeling of quadrotors has remained as an active topic of research for many years due to the difficulty of obtaining a global model valid for all flight conditions. The complex interactions between quadrotor air frame, the actuators and the neighbouring fluid are considered to be the major challenges involved in modeling. An extensive amount of literature suggests several approaches to describe these aerodynamic effects and some of these methods are briefly described in this section.

1.2.1 First Principles Models

The most dominant aerodynamic effects acting on the quadrotor are generally considered to arise from the rotors [9–12]. In [9, 10], this rotor behaviour is modeled by considering the effects of blade flapping. In the work of [12], the implementation of flapping behaviour and induced flow is carried out using blade element theory (BET) and momentum theory (MT). The aerodynamic models obtained with blade element theory and momentum theory are known to be simple and versatile. A common drawback in most theoretical rotor models is that they are derived from the classical helicopter theories which are adjusted for quadrotors. Such an approach according to the author in [13, 14], fails to capture the complex aerodynamic forces and moments of multirotor vehicles. As per the knowledge of the author in [14], no current theoretical models are capable of completely describing the aerodynamics of the quadrotor in the entire operating range. For example, the combined aerodynamic effects resulting from simultaneous lateral and longitudinal motions cannot be determined using the physical knowledge of the system.

1.2.2 Data-Driven Models

The extraction of dynamics from the measured data has been a popular approach for several systems with complicated dynamics. In most available literature, the identification of an unstable and under-actuated system like a quadrotor is performed in closed-loop. Methods including both black-box and grey-box modeling appear to be consistently used for determining the dynamics of multirotor systems.

Black-Box Modeling: In [15, 16], subspace identification methods (SIM) are used to identify linear black-box model structures of quadrotors. The work of [15] obtained unbiased estimates of the continuous-time model for closed-loop hovering data where the reliability of the model is checked using a bootstrap method. Another method of obtaining continuous-time state space models is studied in the work of [17], where the algebraic inversion method is used as the identification

method. Prediction Error Methods (PEM) as an identification criterion are known for their attractive features such as applicability on a wide range of parametric model structures and determining the associated uncertainties in the estimated parameters [18]. The author of the work in [19], uses PEM to determine an ARMAX model structure and in [20] PEM is implemented to determine the parameters of a quadrotor state-space model. Linear black box models derived for quadrotors are unstructured and therefore it cannot be known what information on the dynamics is present in the model. In addition, to capture the highly nonlinear dynamics of a quadrotor, linear data-driven models are insufficient. In [21], a recursive neural network method is used to determine a nonlinear black-box model using a nonlinear ARX model structure. The downside of this approach is that it does not represent the nonlinearity of the quadrotor in a theoretical structure and also such a model is only valid in the region where the identification experiment is performed.

Grey-Box Modeling: To understand the underlying dynamics in a much better sense, grey-box modeling offers the possibility to define the model structure based on the existing physical knowledge of the system and determine the parameters in that model from the measured data. Identification software packages such as SIDPAC and CIFER, developed by research associations are known for parameter estimation of linear quadcopter models. In the work of [22, 23] the SIDPAC identification package is used to determine the parameters of a linear grey-box model. In [23], the parameter estimate of aerodynamic drag and control derivatives are obtained with the SIDPAC parameter estimation algorithm. The author of [24] uses the CIFER package to identify the parameters of structured state-space models. This software determines the parameters of the model by minimizing the cost function in frequency domain. A different approach can be found in [25], where an optimization cost function is designed to identify the parameters of the grey-box model using the data of a previously known black-box model. For this optimization problem, a nullspace-based method is used and the obtained parameter estimates appear to have a very good accuracy. A set of local linear grey-box models linearized at different working points could be used to compose a global quadrotor model but as per the claim of author in [13], a global model obtained in such a way can be quite unreasonable for describing the dynamics of aggressive flights.

Parameter estimation for nonlinear grey-box models is presently considered as one of the well established identification approaches for obtaining an extended quadrotor model in current literature. With all the relevant input and output data available to process, the parameters of the rigid body dynamics as well as the aerodynamics can be determined. For instance, in [26], the author identifies thrust, torque and drag coefficients, moment of inertia and quadrotor mass using a genetic algorithm. In most works [27–30], the focus is on determining aerodynamic effects of the propeller rotation, modeled using blade element theory and identifying the model parameters using suitable identification criteria. For example, in the work of [27], the identification method is based on PEM using a constrained optimization algorithm to refine the initial estimates of the parameters. Utilizing the IMU accelerometer data for identification of aerodynamic forces is another popular approach which is used in the work of [11, 29]. The identified aerodynamic effects are then included into the tracking controller of the quadrotor using feed forward compensation. Improvement in the tracking performance is observed with the inclusion of these aerodynamic effects. Data-driven modeling of the rotor aerodynamics in most work has indeed resulted in improved trajectory tracking capabilities, but for aggressive maneuvers, more complex aerodynamics comes into play. This complex behaviour is suspected to be partially caused by the interaction of the horizontal and vertical components of quadrotor velocity, as stated in the work of [31]. Such a complex aerodynamic behaviour is rarely considered for improving the tracking performance of quadrotors.

1.3 Motivation and Objectives

For aggressive maneuvering of the quadrotor with the controller designed by [32, 33], the closed-loop system performs a stable three-dimensional circular maneuver with a large deviation from the given reference trajectory. This can be explained from the influence of the damping effects, i.e., aerodynamic forces and moments which becomes more prominent when the quadrotor is subjected to faster motion. The controller designed by van den Eijnden in [32, 33] is capable of rejecting these disturbance forces to some extent. However, with increasing magnitude of these motion dependent dynamics, the integral action provided by the controller seems to be insufficient. Tracking controllers can be tuned to either favour disturbance rejection or tracking performance, but not both simultaneously. Since we do not want to make any compromise in performance, the controller needs to be re-designed to take into account the effects of the disturbances. This is achieved by modeling the aerodynamic effects acting on the quadrotor when performing aggressive acrobatic maneuvers.

The extended model with the unconsidered aerodynamic effects is designed by de Kleuver [12], which slightly improves the positions error during simulations. However, there are still some observed inaccuracies in the model with the new dynamics due to the limitations imposed by first principles modeling.

These observations from the previous work form an important basis for the motivation to carry out this research project. The previous research inspires to explore new methods and strategies to significantly improve the tracking performance of the quadrotor for fast makeovers using data-driven modeling techniques.

The objectives of the project can be summarized with the following points:

- Define a suitable grey-box model to determine the disturbances acting on the quadrotor.
- Determine an appropriate identification method to determine the free parameters of the grey-box model structure.
- Re-design the existing tracking controller with the new dynamics such that the resulting closed loop system is stable.
- Conduct experiments with the new controller and evaluate the performance during aggressive maneuvering.

1.4 Problem Formulation

The thesis project aims to improve the trajectory tracking performance of quadrotors by extending the quadrotor model used in the design of the non-linear controller. The disturbance model which is mostly described by aerodynamics needs to be determined through the methods of data-driven modeling.

In the work of [32] and [33], the proposed controller is based on the physical model of the rigid body dynamics and hence any incorporation of the additional dynamics should not alter this structured

non-linear model. Considering these constraints on modeling, the disturbance model in this project is identified through grey-box modeling.

The problem is addressed initially by describing the quadrotor dynamics using the rigid body model and the disturbance model which is to be identified. The center of mass of the quadrotor with respect to the North-West-Up (NWU) inertial frame is denoted by $\rho = [x, y, z]^T$. The linear and angular velocities of the quadrotor, within the body frame are given as, $\nu = [u, v, w]^T$ and $\omega = [p, q, r]^T$. The rotation from the body-fixed frame \mathcal{B} to the inertial frame \mathcal{I} is implemented using the rotation matrix $R \in \mathcal{SO}(3)$. Then the dynamics of the quadrotor model is given as

$$\dot{\rho} = R\nu \quad (1.1a)$$

$$\dot{\nu} = -S(\omega)\nu - gR^T e_3 + \frac{f}{m}e_3 + \frac{F_{aero}}{m} \quad (1.1b)$$

$$\dot{R} = RS(\omega) \quad (1.1c)$$

$$J\dot{\omega} = S(J\omega) + \tau + M_d + M_{aero}, \quad (1.1d)$$

where m is the mass of the quadrotor, $J = \text{diag}([J_x, J_y, J_z])$ is the matrix of moment of inertia, total thrust magnitude $f \in \mathbb{R}$ and total moment vector $\tau \in \mathbb{R}^3$ denote the control outputs for the quadrotor which are given by,

$$\begin{bmatrix} f \\ \tau_1 \\ \tau_2 \\ \tau_3 \end{bmatrix} = \begin{bmatrix} \kappa & \kappa & \kappa & \kappa \\ \kappa l & -\kappa l & -\kappa l & \kappa l \\ -\kappa l & -\kappa l & \kappa l & \kappa l \\ \kappa d & -\kappa d & \kappa d & -\kappa d \end{bmatrix} \begin{bmatrix} \Omega_1^2 \\ \Omega_2^2 \\ \Omega_3^2 \\ \Omega_4^2 \end{bmatrix}, \quad (1.2)$$

in which κ is a parameter based on rotor geometry, l is the distance from center of mass to the rotor centers and d is defined as the rotational drag coefficient. Also Ω_i represent the rotation speed of each i th rotor. The skew-symmetric matrix S is a cross product operator given as,

$$S(a) = -S(a)^T = \begin{bmatrix} 0 & -a_3 & a_2 \\ a_3 & 0 & -a_1 \\ -a_2 & a_1 & 0 \end{bmatrix}. \quad (1.3)$$

In (1.1), F_{aero} , M_{aero} and M_d and represents the disturbance dynamics which are needed to be identified. The terms $F_{aero} = [F_{a,x}, F_{a,y}, F_{a,z}]^T$ and $M_{aero} = [M_{a,x}, M_{a,y}, M_{a,z}]^T$ represent the aerodynamic forces and moments, respectively, acting on the quadrotor. Additionally, $M_d = [M_{gyro,x}, M_{gyro,y}, M_{rot,z}]^T$ represents the moments caused by gyroscopic torques and rotor inertia torque. The main problem of re-designing the tracking controller is then addressed after the identification of the new extended model.

With the dynamics of the extended quadrotor model given in (1.1) and a feasible reference trajectory $(\rho_r, R_r, \nu_r, \omega_r, f_r, \tau_r)$ which satisfies the same dynamics. The error coordinates of the extended quadrotor model on $SE(3)$ will be defined by:

$$\begin{aligned} \tilde{\rho} &= R_r^T(\rho - \rho_r) & \tilde{R} &= R_r^T R \\ \tilde{\nu} &= -\tilde{R}^T S(\omega_r)\tilde{\rho} + \nu - \tilde{R}^T \nu_r & \tilde{\omega} &= \omega - \tilde{R}^T \omega_r, \end{aligned} \quad (1.4)$$

The problem of re-designing the tracking controller can be then be defined by the following statement,

Problem 1.6.1. (Tracking control problem) *Given a feasible reference trajectory $(\rho_r, R_r, \nu_r, \omega_r, f_r, \tau_r)$ for the quadrotor, suitable control laws need to be determined for:*

$$f = f(\rho, R, \nu, \omega, \rho_r, R_r, \nu_r, \omega_r) > 0 \quad (1.5a)$$

$$\tau = \tau(\rho, R, \nu, \omega, \rho_r, R_r, \nu_r, \omega_r), \quad (1.5b)$$

such that for the resulting closed-loop system

$$\lim_{t \rightarrow \infty} \varepsilon(\tilde{\rho}(t), \tilde{R}(t), \tilde{\nu}(t), \tilde{\omega}(t)) = 0, \quad (1.6)$$

where $\varepsilon(\tilde{\rho}, \tilde{R}, \tilde{\nu}, \tilde{\omega}) = \|\tilde{\rho}\| + \|\log \tilde{R}\| + \|\tilde{\nu}\| + \|\tilde{\omega}\|$, is the measure of error.

1.5 Thesis Outline

The contents of the thesis is grouped as follows:

- **Chapter 2: Data Acquisition and Processing**

The data-sets for implementing the identification requires quadrotor states and inputs, which are not directly available from sensor data. This chapter explains the model and processing used for estimation of the attitude, velocity and rotor speed of the quadrotor. Furthermore, the estimation of the aerodynamic forces and moments from the sensors are also described in brief.

- **Chapter 3: Identification of Aerodynamic Models**

Here the Identifications of the disturbance forces and moments is described, which includes the method used for identification, grey-box models defined for aerodynamics of the quadrotor and lastly the estimation of the parameters.

- **Chapter 4: Controller Re-design**

The controller designed by van den Eijnden is re-designed to include the aerodynamic forces and moments. The stability of the position subsystem and the attitude subsystem is derived for the new controller. In addition, the closed loop stability of the entire quadrotor system is proved as well.

- **Chapter 5: Simulation Study**

Chapter 5 illustrates the tracking performance of the re-designed controller for high speed maneuvers through simulation. A comparison of the controller performance is studied with and without the disturbance compensation term.

- **Chapter 6: Conclusion and Recommendations**

The final chapter discusses the conclusions from the obtained results and also mentions the recommendations for further research work.

Chapter 2

Data Acquisition and Processing

In most theoretical models for quadrotor aerodynamics, it is observed that the dynamics are dependent on rotor speed Ω_i , body-fixed velocity ν and angular velocity ω . The available sensors for the AR Drone 2.0 are incapable of directly providing a reliable estimate of these variables, which are required for parameter estimation of the grey-box model. Most quadrotors equipped with Inertial Measurement Units (IMUs), can be used to reconstruct attitude but there are no specific sensors which give an estimate of the body-fixed velocity ν . In Section 2.1 and 2.2 of this chapter, an attitude observer and the position estimates of the quadrotor with respect to inertial frame \mathcal{I} is used to reconstruct the body-fixed velocity ν . The individual rotor speed Ω_i are obtained using the inputs applied to the quadrotor which is described in Section 2.3. Furthermore, the estimation of the aerodynamic forces and moments from IMU sensor data is detailed in Section 2.4.

2.1 Attitude Observer

A good estimate of the quadrotor body-fixed velocity ν , is essential for the identification of many aerodynamic parameters. The smoothed derivatives of the position estimate ρ provide an estimate of the drone's velocity in earth frame \mathcal{I} , but to represent this estimate in the body-fixed frame \mathcal{B} , rotation matrix $R : \mathcal{B} \rightarrow \mathcal{I}$ is needed.

The construction of this rotation matrix $R \in \mathcal{SO}(3)$ requires information on the drone's attitude. To address this issue, an explicit complementary filter with bias correction [34] is proposed to obtain the unbiased attitude information from the IMU gyroscope measurements ω^y and vectorial measurements v_i such as gravitational and magnetic field directions. Unlike direct and passive filters, online algebraic reconstruction of attitude is not required by this observer.

The goal of the non-linear observer is to determine the estimate of the attitude rotation matrix $\hat{R} \in \mathcal{SO}(3)$ in the estimator frame of reference \mathcal{E} and bias estimate \hat{b} such that the error defined by $\tilde{R} = \hat{R}^T R$ and $\tilde{b} = b - \hat{b}$ is driven to $(I, 0)$.

The outputs from the IMU gyroscope, expressed in body-fixed frame \mathcal{B} is represented as follows

$$\omega^y = \omega + b + \eta, \quad (2.1)$$

where $\omega = [p, q, r]^T \in \mathcal{B}$ represents the true values of angular velocity, b denotes a constant or slow time-varying bias and η represents the measurement noise.

Similarly the vectorial data $v_i \in \mathcal{B}$, are given by

$$v_i = R^T v_{0i} + \eta_i, \quad (2.2)$$

where $v_{0i} \in \mathcal{I}$, $i = 1, \dots, n$, represents the inertial directions and η_i is the noise process.

The two body-fixed frame measurements of the inertial directions that can applied to the proposed filter are given by

$$v_a = \frac{a^y}{|a^y|}, \quad v_m = \frac{m^y}{|m^y|}, \quad (2.3)$$

where $a^y, m^y \in \mathcal{B}$ are the gravitational and magnetometer measurements, respectively, obtained from IMU unit. The susceptibility of the magnetometer measurements to electric motors of the quadrotor makes it unreliable and therefore only the accelerometer data is applied to the observer. The kinematics and stability properties of the filter for a single inertial direction data is explained through the following definition and theorem:

Definition 2.1.1. ([34]) Two signals $x(t) : \mathbb{R} \rightarrow M_x$ and $y(t) : \mathbb{R} \rightarrow M_y$ are termed as asymptotically independent if there exists a non-degenerate function $f_t : M_x \times M_y \rightarrow \mathbb{R}$ and any T such that for any $t > T$,

$$f_t(x(t), y(t)) \neq 0, \quad (2.4)$$

in which the term non-degenerate implies that the Hessian of f_t at any point (x, y) is full rank.

Theorem 2.1.1. (Explicit complementary filter, [34], Corollary 5.2) Consider the system kinematics

$$\dot{R} = RS(\omega), \quad (2.5)$$

where $R(t) \in \mathcal{SO}(3)$ and $S(\omega)$ is the cross-product operator on $\omega(t)$ with the measurements defined in (2.1) and (2.2) (for a single measurement $v_1 = v_a$). Let $k_P, k_I > 0$ be the positive gains. Consider the filter kinematics given as

$$\dot{\hat{R}} = \hat{R}(S(\omega^y - \hat{b}) + k_P S(e_{mes})), \quad \hat{R}(0) = \hat{R}_0 \quad (2.6a)$$

$$\dot{\hat{b}} = -k_I e_{mes}, \quad \hat{b}(0) = \hat{b}_0 \quad (2.6b)$$

$$e_{mes} = v_a \times \hat{v}_a, \quad (2.6c)$$

and let $(\hat{R}(t), \hat{b}(t))$ be the solution of (2.6). Assume that $\omega(t)$ is a bounded, absolutely continuous signal and that the pair of signals $(\omega(t), v_a(t))$ are asymptotically independent as per Definition 2.1.1. Let $\hat{v}_a = \hat{R}^T v_{0a}$ be the estimate of the body-fixed measurement $v_a = R^T v_{0a}$. Also, dynamics of the estimator \hat{v}_a is given by

$$\dot{\hat{v}}_a = -S(\omega^y - \hat{b} + k_P v_a \times \hat{v}_a) \hat{v}_a. \quad (2.7)$$

Define:

The error variables are defined as, $\tilde{R} = \hat{R}^T R$ and $\tilde{b} = b - \hat{b}$. The set $\mathbb{U}_1 \in \mathcal{SO}(3) \times \mathbb{R}^3$ is given by,

$$\mathbb{U}_1 = \{(\tilde{R}, \tilde{b}) : v_{0a}^T \tilde{R} v_{0a} = -1, \tilde{b} = 0\} \quad (2.8)$$

Then:

- 1) Under the closed-loop filter dynamics, the set \mathbb{U}_1 is forward invariant and unstable for some ϵ -neighborhood of \mathbb{U}_1 given by,

$$\mathbb{D} = \{(\tilde{R}_*, \tilde{b}_*) : d((\tilde{R}_*, \tilde{b}_*), \mathbb{U}_1) < \epsilon\} \quad (2.9)$$

in which $d((\tilde{R}_*, \tilde{b}_*), \mathbb{U}_1)$ is the minimum distance between $(\tilde{R}_*, \tilde{b}_*)$ and set \mathbb{U}_1 defined by,

$$d((\tilde{R}_*, \tilde{b}_*), \mathbb{U}_1) = \inf_{\tilde{R}, \tilde{b} \in \mathbb{U}_1} (1 - v_{0a}^T \tilde{R}_*^T \tilde{R} v_{0a} + \|\tilde{b}_* - \tilde{b}\|) \quad (2.10)$$

- 2) For equilibrium point $(I, 0)$ of (\tilde{R}, \tilde{b}) , the estimate (\hat{v}_a, \hat{b}) is locally exponentially stable to (v_a, b) .
- 3) The trajectory $(\hat{v}_a(t), \hat{b})$ converges to the trajectory $(v_a(t), b)$ for almost all initial conditions $(\tilde{R}_0, \tilde{b}_0) \notin \mathbb{U}_1$.

The architecture of this non-linear attitude observer is shown in Figure 2.1. In the block diagram for filter, the term $\omega^y - \hat{b} + k_P v_a \times \hat{v}_a$ is denoted by $\hat{\omega}$. The PI compensation of the explicit complementary filter is controlled using the gains k_P and k_I . In Appendix A, the proposed observer is simulated for suitable choice of gains k_P and k_I .

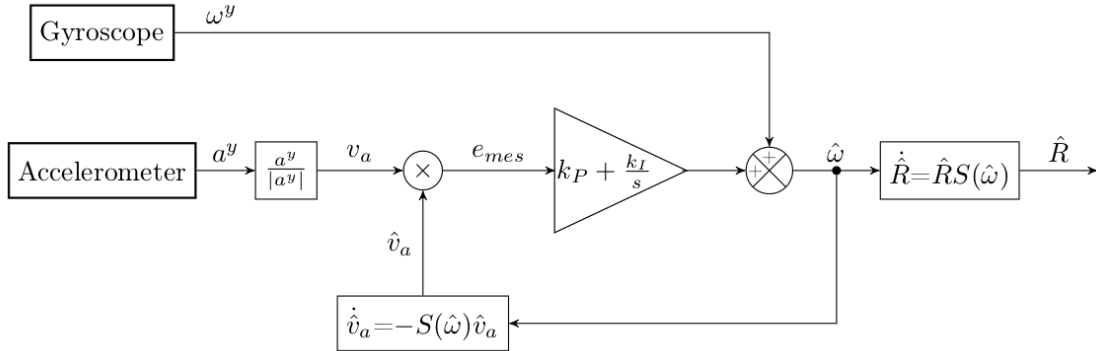


Figure 2.1: Block diagram of the explicit complementary filter with bias correction.

2.2 Velocity Estimation

The xy -position estimates of the drone is obtained from the external camera which is sampled at the rate of 30 Hz with a delay of 0.1s. The state observer designed by N. Jeurgens in [35] provides the estimate of z -position in inertial frame using the roll ϕ and pitch θ angles computed with an attitude observer and the body-fixed frame z -position estimates acquired from the altimeter outputting at 25 Hz. In [35], a dual linear Kalman filter is proposed which provides reliable estimate of roll ϕ and pitch θ angles and therefore the z -position estimate in \mathcal{I} is also reliable. However, this attitude observer provides erroneous yaw angle ψ estimates of the quadrotor.

The proposed explicit complementary filter in Section 2.1 is instead used to construct the rotation matrix R to represent the $\rho \in \mathcal{I}$ of the quadrotor in body-fixed frame \mathcal{B} using

$$\nu = R^T \dot{\rho}, \quad \nu \in \mathcal{B}. \quad (2.11)$$

The position estimates of drone samples data at a lower rate compared to the attitude information which is sampled 400 Hz. In order to use all the data to control the drone, the model used for experiments uses an update mechanism [32, 35] for the position estimates. This results in quantized position data from holding the samples at different intervals.

The process of filtering of such quantized signals from moving average method results in smoothing out of important information in the signals. Hence, a differentiation filter known as Savitsky Golay filter [48, 49] is used to compute the smooth derivatives of position ρ and then use the expression in (2.11) to compute the body-fixed velocity ν . The Savitsky Golay filter is capable of preserving most of the important information on the signals and also rapidly compute derivatives of the signals in time domain using the properties of convolution. The smoothed position derivatives obtained using this differentiation filter is detailed in Appendix B.

2.3 Rotor Speed Estimation

System inputs, thrust f and the torques $\tau = [\tau_1, \tau_2, \tau_3]^T$ are computed by the controller to follow a given trajectory. A relation is then used to calculate the thrust T_i required by each rotor for the given inputs given by,

$$\begin{bmatrix} f \\ \tau_1 \\ \tau_2 \\ \tau_3 \end{bmatrix} = \begin{bmatrix} 1 & 1 & 1 & 1 \\ l & -l & -l & l \\ -l & -l & l & l \\ d & -d & d & -d \end{bmatrix} \begin{bmatrix} T_1 \\ T_2 \\ T_3 \\ T_4 \end{bmatrix}, \quad (2.12)$$

where l is the distance from the rotors to the center of mass, and d is the rotational drag coefficient.

In the thesis report of N. Jeurgens [35], the functions representing the quadratic relationship between individual rotor thrust T_i and PWM values $P_{W,i}$ is determined using a force transducer, given by:

$$\begin{bmatrix} T_1 \\ T_2 \\ T_3 \\ T_4 \end{bmatrix} = \begin{bmatrix} 1.5618 \cdot 10^{-4} P_{W,1}^2 + 1.0395 \cdot 10^{-2} P_{W,1} + 0.13894 \\ 1.8150 \cdot 10^{-4} P_{W,2}^2 + 8.7242 \cdot 10^{-3} P_{W,2} + 0.14425 \\ 1.3478 \cdot 10^{-4} P_{W,3}^2 + 7.3295 \cdot 10^{-3} P_{W,3} + 0.11698 \\ 1.4306 \cdot 10^{-4} P_{W,4}^2 + 5.7609 \cdot 10^{-3} P_{W,4} + 0.13362 \end{bmatrix}. \quad (2.13)$$

Then the PWM values $P_{W,i}$ determined by the above expression are supplied as motor inputs to the quadrotor. It is observed that there exists a linear relationship between the PWM values $P_{W,i}$ supplied to the motors and the individual rotor speed Ω_i of the quadrotor [36]. This relationship was experimentally determined in [35] using an RPM counter, given by:

$$\begin{bmatrix} \Omega_1 \\ \Omega_2 \\ \Omega_3 \\ \Omega_4 \end{bmatrix} = \begin{bmatrix} 3.7503 P_{W,1} + 132.7387 \\ 3.7123 P_{W,2} + 131.5018 \\ 3.7891 P_{W,3} + 132.7387 \\ 3.7380 P_{W,4} + 132.2209 \end{bmatrix}. \quad (2.14)$$

The above expression is used for determining the individual rotor speeds Ω_i of the quadrotor which is a crucial data for implementing the identification procedures.

2.4 Extraction of Aerodynamic Forces and Moments

When considering the forces acting on the body-fixed frame of the quadrotor, the translational dynamic equations are given as

$$m\dot{\nu} = -mS(\omega)\nu + \sum F_{ext}, \quad (2.15)$$

where $mS(\omega)\nu$ represents the Coriolis term which is regarded as the fictitious internal force. The term $\sum F_{ext}$ represents the sum all the external forces which includes the gravitational force and all the aerodynamic forces acting on the quadrotor, given as

$$\sum F_{ext} = -mR^T g e_3 + f e_3 + F_{aero}, \quad (2.16)$$

where the thrust f and all the other aerodynamic forces F_{aero} together represent the total aerodynamic forces acting on the quadrotor.

The expression for IMU accelerometer which measures in body-fixed frame \mathcal{B} , is given as [9],

$$ma^y = mR^T(g e_3 + \ddot{\rho}), \quad (2.17)$$

where the internal force described by the Coriolis term is not measured by this sensor since it measures only the externally applied forces rather than the resultant forces acting on the body-fixed frame as mentioned in [31, 37, 38].

The measurement of force $mR^T\ddot{\rho}$ is not directly sensed by the accelerometer, in reality this is estimated from the externally applied aerodynamic forces. Also, the external thrust f in z -direction is also not directly measured, but during flight this force is equal to the gravitational force which is given by $mR^T g$. So (2.17) can written as:

$$ma^y = f e_3 + F_{aero}. \quad (2.18)$$

With this expression, the time signals of the total aerodynamic forces can directly be obtained for parameter estimation of suitable grey-box models.

The rotational dynamics of the quadrotor is defined as,

$$J\dot{\omega} = S(J\omega)\omega + \tau + M_d + M_{aero}, \quad (2.19)$$

where the summation of M_d and M_{aero} represent the total disturbance moment acting on the drone. Unlike the accelerometer, the gyroscope of the IMU sensor measures the effect of the resultant moments rather than just the externally applied moments. With (2.19) and the IMU gyroscope angular velocity ω^y , the disturbance moments can be isolated by rearranging the terms as

$$J\dot{\omega}^y - S(J\omega^y)\omega^y - \tau = M_d + M_{aero}. \quad (2.20)$$

2.5 Concluding Remarks

The datasets required for the identification are either not directly available or are corrupted with noise and bias. This chapter describes the approaches used to obtain the datasets from the available sensors for the quadrotor flight experiments. The representation of the quadrotor velocity in the

body-fixed frames requires information on the attitude estimates. An explicit complementary filter with bias correction is used to reconstruct the attitude information of the drone from the IMU gyroscope and accelerometer measurements. The derivatives of the external camera position estimates are used to estimate the quadrotor velocity in the inertial frame. A specific differentiation filter known as the Savitsky Golay filter is used to compute the derivatives of the quantized position data. This filter is known to preserve most of the significant information on quadrotor velocity without too much smoothing. Another important data is the quadrotor rotor speed which is estimated using the PWM inputs supplied to the motors of the quadrotor. The linear mapping of the rotor speeds to the PWM inputs used for the estimation of rotor rotation speed. Lastly, the measurements of the aerodynamic forces and moments are acquired from the IMU accelerometer and gyroscope data, respectively. It is assumed that the accelerometer data captures only the external forces measurement due to which the internal forces are neglected. However, the gyroscope sensor measures the net resultant moment acting on the vehicle and therefore all the internal and external moments need to be considered for isolating the data on aerodynamic and other disturbance moments.

Chapter 3

Identification of Aerodynamic Models

In this chapter, the identification of the aerodynamic models is performed. The complex aerodynamic effects involving the quadrotor frame, rotors and the surrounding air is difficult to model with the currently known theoretical models [9–12]. Such models usually describe the aerodynamics of quadrotors by only considering the rotor flapping behaviour and induced flow. As stated in the work of [31, 36], complex interactions between lateral and longitudinal linear velocity of the quadrotor is also crucial to capture the aerodynamics of the system. Identification methods offer the possibility to model such complex dynamics which usually cannot be explained by the physical models.

The outputs of the IMU sensor are widely used to identify the aerodynamic forces and moments acting on the body-fixed frame of the quadrotor [11, 29, 31, 36]. This simple approach enables to identify the aerodynamic effects in such a way that they can be represented together with the known theoretical rigid body model. Furthermore, since the aerodynamic models are identified with respect to the body-fixed frame \mathcal{B} , there are no additional rotation matrices introduced in the quadrotor model. The identification procedure is explained through the schematic representation given in Figure 4.1.

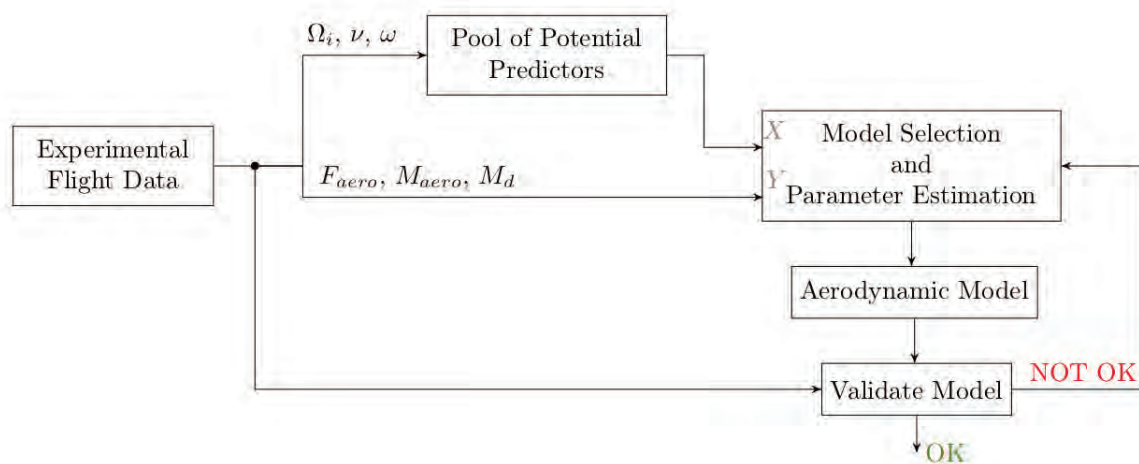


Figure 3.1: Schematic illustration of the identification method.

The identification procedure entails several steps from processing the flight data till validation of

the suitable model. The different stages crucial to the identification process is explained in brief through the following points:

- **Experiment data**

To capture most of the system dynamics in the model, the experiments conducted should sufficiently excite the necessary variables. For instance, to determine the strong coupling between the rotor speed Ω_i , body linear velocity ν and angular velocity ω of the aerodynamic model, the experiments should be performed to simultaneously excite all the independent variables. The determination of the independent variables Ω_i , ν and ω and the response variables F_{aero} , M_{aero} and M_d is described in detail in the previous chapter.

- **Potential predictors**

The combination of the independent variables are used to form the potential predictors for the model. In the case of the aerodynamic model, polynomial functions are formed with this combination. The potential predictors are determined with the known theoretical models for quadrotor aerodynamics. In addition, polynomial functions to account for the other aerodynamic effects not explained by the physical models are also formed with the variables. The pool of predictors is defined in the further sections of this chapter to fit the aerodynamic forces F_{aero} and disturbance moments M_{aero} and M_d . In Section 3.2 and 3.3 the model structure for thrust force (\hat{F}_z) and drag force ($\hat{F}_{a,x}$ and $\hat{F}_{a,y}$) are defined. Similarly, the grey-box models for roll and pitch moment (\hat{M}_x and \hat{M}_y) are defined in Section 3.4 and the structure for yaw moment model (\hat{M}_z) is given in Section 3.5. Furthermore, in Section 3.6 it is briefly explained how the aerodynamic forces and moments varies with quadrotor air speed.

- **Model selection**

The sum of all the potential predictors defines the model set for carrying out the identification. It is important to determine only the best set of predictors to fit the response variables F_{aero} , M_{aero} and M_d without any over fitting. To implement this, a model selection criterion is applied using Least Absolute Shrinkage and Selection Operator (LASSO). The criterion is applied using Least Angle Regression (LAR) algorithm proposed by Efron et al. [39] and is explained in Section 3.1. Once, the right set of predictors are selected and the free parameters are estimated the model for performing validation test is defined.

3.1 Model Selection

Consider the model selection problem defined by the following linear-in-parameters regression model,

$$y = X\Theta + \epsilon, \quad (3.1)$$

where $y \in \mathbb{R}^N$ represents the response variable with N data points. The regressors matrix is given by, $X = [\varphi_0, \varphi_1, \varphi_2, \dots, \varphi_m] \in \mathbb{R}^{N \times m}$, which contains the constant predictor φ_0 in the first column and φ_i which represents the i th candidate predictor, where $i = 1, 2, \dots, m$. The vector $\Theta = [\Theta_1, \Theta_2, \dots, \Theta_m] \in \mathbb{R}^m$ represents the parameter vector and ϵ is the residue between measurement data and output of the model.

For identification of the aerodynamic model, the response variable y is given by the measurements of F_{aero} , M_{aero} and M_d . Also, the matrix X consists of the predictors formed with the independent variables Ω_i , ν and ω .

Let the matrix X represent the dictionary of the m potential predictors to fit the response variable y . In model identification, it is often redundant to use the complete set of predictors defined in X . Thus, our model selection problem is equivalent to determining a full dimensional subset $X_P = [\zeta_0, \zeta_1, \dots, \zeta_P] \in \mathbb{R}^{N \times P}$ of $P \leq m$ predictors from the library of X , with constant predictor $\zeta_0 = \varphi_0$. Then the system response variable y can be acceptably approximated using a linear combination of $\zeta_0, \zeta_1, \zeta_2, \dots, \zeta_P$, given by

$$\begin{aligned} y &= \theta_0 \zeta_0 + \theta_1 \zeta_1 + \dots + \theta_P \zeta_P + \epsilon \\ &= X_P \theta + \epsilon. \end{aligned} \quad (3.2)$$

The problem of model selection in (3.1) is confronted by implementing Least Absolute Shrinkage and Selection Operator (LASSO), which is method for regularizing a least squares regression. The LASSO method fits the linear model, given by,

$$\hat{y} = \sum_{i=1}^m \varphi_i \Theta_i \quad (3.3)$$

with the constant predictor term φ_0 excluded, to solve the optimization problem,

$$\hat{\Theta} = \min_{\Theta} \|y - \hat{y}\|^2 \quad \text{subject to} \quad \sum_{i=1}^m |\Theta_i| \leq s, \quad (3.4)$$

where $\|\cdot\|$ is the L2 norm and $s \geq 0$ is the tuning shrinkage parameter used to select the number of predictors to the model. A sufficiently large value of s , will produce the ordinary least square solution for (3.4) and smaller values shrinks some estimates of Θ to zero.

The expression given in (3.4), was earlier solved using quadratic programming which was computationally cumbersome. Therefore, we use the Least Angle Regression (LAR) algorithm proposed by Efron et al. [39] which implements the LASSO optimization problem with a small modification. Such an implementation determines the solutions for LASSO for all shrinkage parameter s . The LAR algorithm with modification for LASSO is shown in Algorithm 3.1 which is based on the work of [41].

Since the given algorithm will add one predictor with every step, the Bayesian Information Criterion (BIC) is used to terminate the LAR code. Assuming the LAR algorithm has added p predictors after n steps to the model, then the BIC criterion is defined by,

$$BIC_n = N \ln (RSS_n/N) + p \ln(N), \quad (3.5)$$

where RSS_n is the residual sum of squares given by $\|y - \hat{y}\|^2$. Then the following condition is used as a satisfactory model selection stopping criterion [40],

$$|BIC_{n-1} - BIC_n| < \epsilon_{crit}, \quad (3.6)$$

in which the value of ϵ_{crit} decides how many predictors are to be included in the model.

Algorithm 3.1 Least Angle Regression (LAR) with LASSO modification**Initialize:**

- 1: Standardize the predictors φ_i , $0 < i \leq m$ to keep mean $\mu = 0$ and variance $\sigma = 1$, except the constant predictor term φ_0 . Set coefficients $\Theta_1, \Theta_2, \dots, \Theta_m = 0$.
- 2: Find the first predictor most correlated to response y and determine the residue, $r = y - \hat{y}$, where \hat{y} is the least square estimation of y .

Procedure:

- 3: Excluding the first predictor, find a predictor φ_j most correlated with r .
- 4: Increase coefficient Θ_j from zero towards its least-squares coefficient $\langle \varphi_j, r \rangle$ until some other candidate φ_k has as much correlation with the current residual as φ_j .
- 5: Move coefficient (Θ_j, Θ_k) in the direction determined by joint least squares coefficient of the present residual on (φ_j, φ_k) , until some other candidate φ_l has as much correlation with the current residual.
- 6: **LASSO modification:** Continue this pattern and if some non-zero coefficient reaches zero, remove it from the active set and recompute the present joint least squares direction.

Stop Criterion:

- 7: The above procedure is terminated when the BIC stopping criterion in (3.6) is met.

Once the model with p most essential predictors are selected using Algorithm 3.1, the output model is estimated by also including the constant predictor term (for bias), given by

$$\begin{aligned}\hat{y} &= \hat{\theta}_0 \zeta_0 + \hat{\theta}_1 \zeta_1 + \dots + \hat{\theta}_P \zeta_P + \epsilon \\ &= X_P \hat{\theta}\end{aligned}\tag{3.7}$$

where the value of $\hat{\theta}$ is estimated by the original least squares (OLS) solution, defined by

$$\hat{\theta} = (X_P^T X_P)^{-1} X_P^T y\tag{3.8}$$

3.2 Thrust Force Model

In this section, the structure of the thrust model \hat{F}_z is defined using the known quadrotor aerodynamic theories. The purpose of this model is to capture the resultant force acting on the z -direction of the quadrotor. The thrust force excluding the drag forces denoted by \hat{T} , is first modelled by considering the following components of forces:

- The thrust generated by the propellers.
- The force due to thrust variance effect which is caused by translational lift and rotor induced velocity [10]. Effective translational lift is the aerodynamic force which results from the quadrotor performing climbing and descending maneuvers. The other effect is caused by the inflow of air through the rotor disk known as the rotor induced velocity.

Assumption 3.2.1 For purposes of identification the following assumptions are considered:

- i) The local rotor velocities, $\nu_i = [u_i, v_i, w_i]^T \in \mathcal{B}$ in the body frame of all the four rotors are identical.
- ii) The induced velocity $\nu_{in,i}$ of each rotor is assumed to equal to each other as well.

The thrust forces of the i th rotor is hence expressed by [42]:

$$T_i = \frac{\rho_a a B c \Omega_i^2 R_{ra}^3}{2} \left(\frac{\theta_r}{3} + \frac{V_i^2 \cos^2 \alpha \theta_r}{2 \Omega_i^2 R_{ra}^2} + \frac{\nu_{in,i} - V_i \sin \alpha}{2 \Omega_i R_{ra}} \right) \quad (3.9)$$

where ρ_a is the density of air, a is the lift curve slope of blade profile, B refers to the number of blades, c is the blade chord, R_{ra} indicates the rotor radius, θ_r is the rotor pitch angle, $V_i = \|\nu_i\|$ is the resultant magnitude of the i th rotor velocity, α is the angle of attack between coming air flow and rotor disk and $\nu_{in,i}$ is the induced velocity of the i th rotor.

Now, the resultant speed V_i of rotor i of the quadrotor is a function of the horizontal and vertical body-fixed velocities of the quadrotor. Hence, by substituting the following terms,

$$V_i \cos \alpha = \sqrt{u_i^2 + v_i^2}, \quad V_i \sin \alpha = w_i, \quad (3.10)$$

in the expression given for T_i in (3.9), we get

$$T_i = \frac{\rho_a a b c \Omega_i^2 R_{ra}^3}{2} \left(\frac{\theta_r}{3} + \frac{(u_i^2 + v_i^2) \theta_r}{2 \Omega_i^2 R_{ra}^2} + \frac{\nu_{in,i} - w_i}{2 \Omega_i R_{ra}} \right) \quad (3.11)$$

All the constants for T_i can be lumped together for simplicity and therefore the model for the total rotor generated thrust in the body-fixed frame can be given as,

$$\hat{T} = \sum_{i=1}^4 T_i = \kappa_0 \sum \Omega_i^2 + \kappa_1 (u^2 + v^2) + \kappa_2 (\nu_{in} - w) \sum \Omega_i \quad (3.12)$$

in which κ_0 , κ_1 and κ_2 are the constant parameters. The term $\sum_{i=1}^4$ will be simply represented by \sum in further expressions. The total induced velocity ν_{in} during translational flight in the quadrotor body-fixed frame is given by [10],

$$\nu_{in} = \frac{v_h^2}{\sqrt{u^2 + v^2 + (v_{in} - w)^2}}, \quad (3.13)$$

where v_h is the induced velocity of the quadrotor during hovering. The resultant force acting in the z -direction of the quadrotor is then given by,

$$\begin{aligned} \hat{F}_z &= \hat{T} + D_z \\ &= \kappa_0 \sum \Omega_i^2 + \kappa_1 (u^2 + v^2) + \kappa_2 (\nu_{in} - w) \sum \Omega_i + D_z, \end{aligned} \quad (3.14)$$

in which D_z represents all the drag forces in the z -direction of the body-frame.

When the drone flight experiments are conducted to only hover at a certain a height, the resultant force in z -direction given in (3.14) reduces to the following,

$$\hat{F}_{hov} = \kappa_0 \sum \Omega_i^2 + \kappa_2 \nu_h \sum \Omega_i, \quad (3.15)$$

where the components of body-fixed velocities $\nu = 0$, during hovering at a stationary point. In the above expression the induced velocity ν_{in} becomes equal to the hovering induced velocity ν_h , which can be inferred from (3.13). In the work of [30], it is empirically proven that the induced velocity during hovering has a linear relationship with the rotor speed, which can be expressed as,

$$\nu_h = d_h \sum \Omega_i, \quad (3.16)$$

where d_h is a constant parameter. Hence the expression for hovering model \hat{F}_{hov} in (3.15) can be written as,

$$\hat{F}_{hov} = \kappa_0 \sum \Omega_i^2 + \kappa_2 d_h \left(\sum \Omega_i \right)^2 \approx (\kappa_0 + \kappa_2) \sum \Omega_i^2 = \kappa \sum \Omega_i^2, \quad (3.17)$$

in which the constants κ_0 and κ_2 are lumped together and represented by κ . Here we have obtained an approximate model for \hat{F}_{hov} which has a direct mapping to the term $\sum \Omega_i^2$. To determine the hovering parameter κ of this model it is required to perform several hovering experiments with the quadrotor. However, drones operating near the ground can suffer from varying effects of the induced velocity which is known as the ground effect. It is required to perform hovering experiments at height z from the ground which satisfies the condition $z/R_{ra} > 0.5$ [43], where the variation of the induced velocity effect becomes negligible.

The closed-loop hovering flight experiments are performed using the controller designed in [32], for the position reference trajectory given by,

$$\rho_r = \begin{bmatrix} 0 & 0 & z_r \end{bmatrix}^T, \quad z_r = 1\text{m} \quad (3.18)$$

The parameter κ is computed using recursive least squares using the the individual rotor speed Ω_i data and the measurement for hovering thrust force F_{hov} is obtained from the accelerometer measurement in z -direction. Figure 3.2 shows the sequential estimation of parameter κ with the dataset formed with eight different hovering flight experiments. The estimate of parameter κ from each hovering experiment is presented in Appendix C and the detailed explanation to the applied recursive least squares method is given in Appendix D.

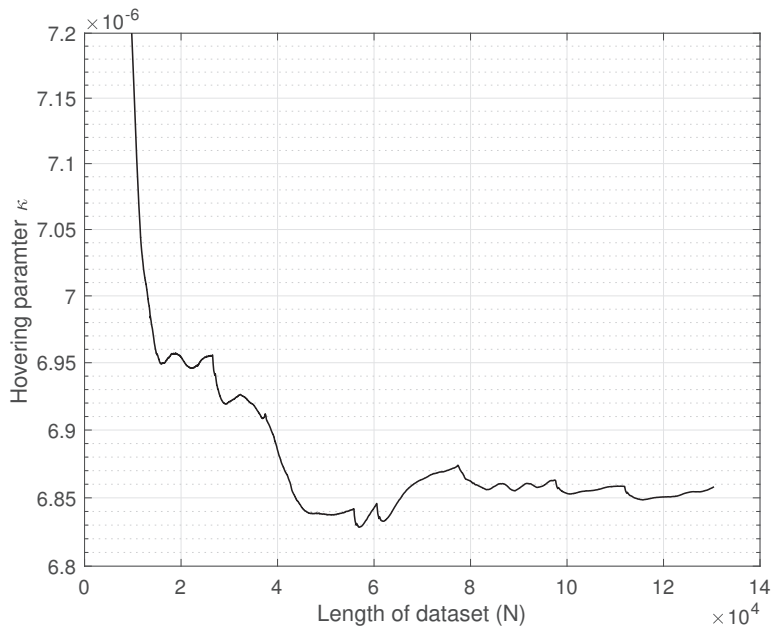


Figure 3.2: Recursive estimation of parameter κ from combined data of eight different hovering flight experiments.

During experiments for hovering data, the quadrotor was not able to hover motionless for a long period and therefore multiple datasets were acquired for estimation of parameter κ . It is observed

in Figure 3.2 that after $N = 8000$, the parameter value becomes more consistent. The final value obtained for the hovering parameter is $\kappa = 6.858 \cdot 10^{-6} \text{ N rad}^{-2}\text{s}^2$.

The remaining terms of the model \hat{F}_z given in (3.14) can be represented by forming polynomial functions with independent variables of ν and $\sum \Omega_i$ [31]. Then the set of model predictors are given as:

$$\begin{aligned} \hat{F}_{z_{set}} = & \hat{F}_{hov} + \Theta_0 + \Theta_1(u^2 + v^2) + \Theta_2w \sum \Omega_i + \Theta_3w^2 \sum \Omega_i + \Theta_4u \sum \Omega_i + \\ & \Theta_5v \sum \Omega_i + \Theta_6uw^2 + \Theta_7vw^2 \end{aligned} \quad (3.19)$$

where \hat{F}_{hov} is the estimated hovering model which remains fixed in the set and Θ_i for $i = 0, 1 \dots 7$, are the unknown free parameters with Θ_0 being the parameter of constant predictor or bias. In the above expression, the third and fourth term of the polynomial model resemble the ones given in (3.14). The terms $w^2 \sum \Omega_i$, $u \sum \Omega_i$ and $v \sum \Omega_i$ partly represent the effects of the induced velocity term ν_{in} . Using first principles models, it is difficult to determine ν_{in} for the thrust model, but our proposed identification method can capture its effects in the grey-box model. Furthermore, uw^2 and vw^2 represent the aerodynamic drag forces acting in z -direction which is represented by D_z in (3.14). These terms take into consideration the coupling of horizontal and vertical motion of the quadrotor.

Now, the model selection criterion from the previous section is implemented to determine the most essential predictors in model set $\hat{F}_{z_{set}}$ given in (3.19). This selection criterion is not only used to avoid overfitting but also to limit the number of model terms for the final quadrotor model. For determining the parameter κ , the hovering trajectory in (3.18) was chosen to eliminate all the other disturbance effects. Similarly, to determine all the free parameters in the model, the flight trajectory should excite all the independent variables of body-fixed velocity ν and rotor speed Ω_i simultaneously. Here, we use the 3D fast trajectory for the flight experiment defined by the following reference position,

$$\rho_r(t) = [\cos(a_t t) \quad \sin(a_t t) \quad 1.5 + \sin(a_t t)]^T \quad (3.20)$$

where $a_t=1$ for fast 3D circular maneuver. The IMU accelerometer flight data for z -direction is then collected from this experiment to get the measurement of aerodynamic force F_z . By using this measurement as the response variable and the model set for $\hat{F}_{z_{set}}$ defined in (3.19), the model selection algorithm is applied with $\epsilon_{crit} = 400$ for restricting the number of model terms.

Figure 3.3 shows the evolution of the function $BIC_{n-1} - BIC_n$ (in blue) with respect to n iteration steps of the selection method. It is observed in the figure that after $n = 4$, the value drops below the chosen critical value of ϵ_{crit} (dashed in black). It can be also seen that after $n = 4$, the values go in a non-increasing fashion except at $n = 7$. This is because at iteration step of $n = 7$, the coefficient of one of the model terms already existing in the model shrinks to zero. As per Algorithm 3.1, the LASSO modification step removes the model term whose coefficient value reaches zero and recomputes the present joint least square direction. The selection algorithm then adds another more correlated model term to the model set in the same step of $n = 7$.

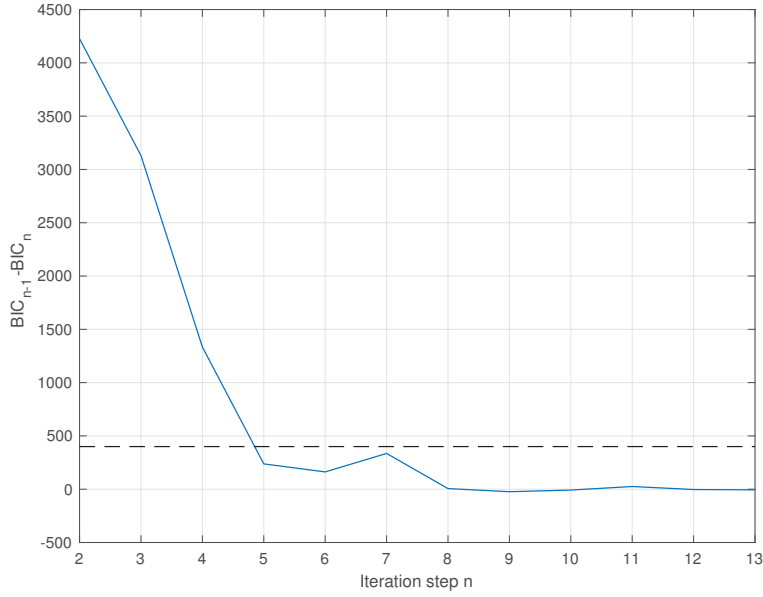


Figure 3.3: Model selection algorithm applied for model set \hat{F}_{zset} with chosen ϵ_{crit} (dashed in black)

For the choice of the ϵ_{crit} , the model terms for up to $n = 4$ steps are only considered. The resulting output model with $p = 4$ selected model terms and the bias term is given by:

$$\hat{F}_z = \hat{F}_{hov} + \hat{\theta}_1 + \hat{\theta}_2(u^2 + v^2) + \hat{\theta}_3 u \sum \Omega_i + \hat{\theta}_4 v \sum \Omega_i + \hat{\theta}_5 w \sum \Omega_i \quad (3.21)$$

in which the free parameters $\hat{\theta}_i$ with $i = 1, \dots, 5$, are estimated using the original least squares solution given in (3.8). The value of estimated parameters are given in Table 3.1 which are sorted as per the most to least relevant predictor terms of the model.

| Model Predictor | Parameter ($\hat{\theta}$) | Estimated Value | Units |
|-------------------|------------------------------|-----------------------|---|
| $w \sum \Omega_i$ | $\hat{\theta}_5$ | $-3.91 \cdot 10^{-4}$ | $\text{N}(\text{m}\cdot\text{rad})^{-1} \text{s}^2$ |
| $v \sum \Omega_i$ | $\hat{\theta}_4$ | $-2.17 \cdot 10^{-5}$ | $\text{N}(\text{m}\cdot\text{rad})^{-1} \text{s}^2$ |
| $u \sum \Omega_i$ | $\hat{\theta}_3$ | $-1.55 \cdot 10^{-4}$ | $\text{N}(\text{m}\cdot\text{rad})^{-1} \text{s}^2$ |
| $u^2 + v^2$ | $\hat{\theta}_2$ | $-1.46 \cdot 10^{-1}$ | Nm^{-2}s^2 |
| 1 | $\hat{\theta}_1$ | $-2.98 \cdot 10^{-2}$ | - |
| NMSE fit | | 85.86 % | |

Table 3.1: Estimated value of the free parameters for thrust model \hat{F}_z (sorted from most to least relevant).

In Table 3.1, the % goodness of fit of the obtained model on to the estimation data set is evaluated

by computing the Normalized mean square error (NMSE), given by

$$\text{fit}\% = \left(1 - \frac{\|y - \hat{y}\|^2}{\|y - \bar{y}\|^2}\right) \times 100, \quad (3.22)$$

where $\|\cdot\|$ represents the 2-norm of vector and \bar{y} is the mean value of the measurement or reference data y . Table 3.1 shows that the most relevant or correlated predictor for thrust model is the term which involves the independent variable $\sum \Omega_i$. This is understandable since in z -direction the air induced with propeller rotation contribute the most towards the aerodynamic effects acting on the quadrotor. The predictor term $v^2 + u^2$ representing the effective translational lift seems to contribute as well in the aerodynamic model of F_z .

It is however also noticed that the effect of terms uv^2 and uv^2 , which takes into account the drag forces in (3.19) had no significant effect on the quadrotor aerodynamics in z -direction. As per the work of [36], resultant airspeed V of the quadrotor should be greater than 2 m/s to model the complex aerodynamic effects. Since, the drone experiments are conducted at normal room wind speed, some of the disturbance dynamics cannot be identified and incorporated to the present model.

In Figure 3.4, the fit of the estimated model on the validation data is illustrated for the same 3D fast trajectory defined in (3.20). The performance of the estimated model \hat{F}_z is evaluated by also comparing it with the simple hovering thrust model \hat{F}_{hov} .

As seen in the Figure 3.4, the hovering thrust model \hat{F}_{hov} lags behind the measurement of force F_z and also overestimates the magnitude due to negligence of the damping effects. The aerodynamic force model \hat{F}_z seems to predict the magnitude of the measurement much better and also the phase difference between the measurement F_z and the model \hat{F}_z is also reduced. A validation fit of 70.53% is obtained for the estimated model with estimation fit of 85.86%. To bring the validation fit results much more closer to estimation fit, the parameter estimates needs to be recomputed with longer identification dataset.

It is to be noted that the number of mode predictor terms can be further increased to improve the estimation and validation fit without any overfitting. Since the additional disturbance dynamics terms for the non-linear controller has to be limited, only the few most relevant predictors are included.

In the model selection criterion by adjusting the value of ϵ_{crit} given in (3.6), the number of model predictors from the model set of \hat{F}_z can be controlled. In the next section for modeling drag forces, the choice of ϵ_{crit} is chosen to be even smaller.

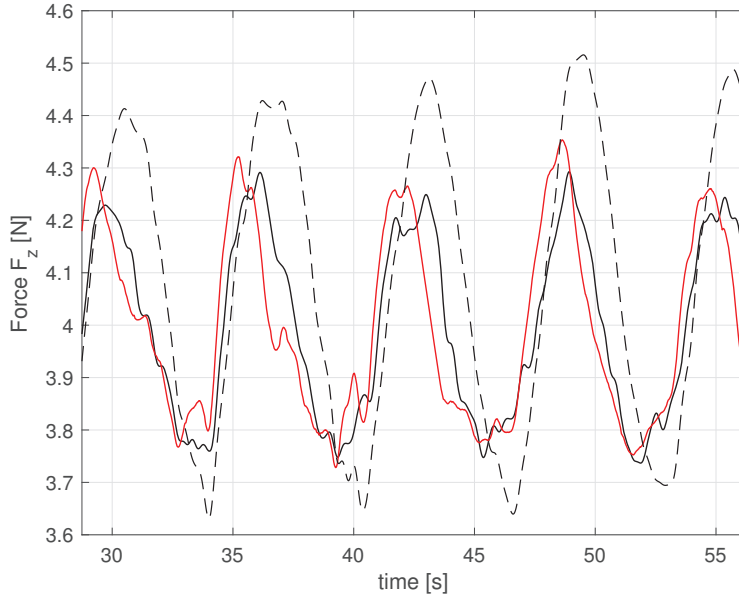


Figure 3.4: Validation fit results on the measurement F_z (black) with hovering model \hat{F}_{hov} (dashed) and identified thrust model \hat{F}_z (red) of NMSE fit - 70.53%.

3.3 Drag Force Model

The aerodynamic forces acting in x and y direction of the quadrotor is modeled in this section. Disturbance dynamics in the horizontal direction of the drone are mostly caused by the aerodynamic drag forces. The Assumption 3.2.1 for local rotor velocities and induced velocities is taken into consideration for the drag force models as well. To model $F_{a,x}$ and $F_{a,y}$, we consider the following horizontal forces:

Blade flapping effect :

When the tip-path-plane of the rotor blade during translating horizontally through air tilts back to balance the aerodynamic forces with its flexibility, the rotor thrust is tilted back which leads to a horizontal force. This horizontal drag force on rotor i due to blade flapping is expressed as [9],

$$D_{Bf,i} = T_{h,i} A_{flap} \frac{V_{H,i}}{\Omega_i R_{ra}}, \quad (3.23)$$

where $T_{h,i}$ represents the nominal hovering thrust for rotor i , $V_{H,i} = [u_i, v_i, 0]^T \in \mathcal{B}$ is the velocity of the rotor in the x - y plane and A_{flap} is given by,

$$A_{flap} = \begin{bmatrix} A_{1c} & -A_{1s} & 0 \\ A_{1s} & A_{1c} & 0 \\ 0 & 0 & 0 \end{bmatrix}, \quad (3.24)$$

in which A_{1c} and A_{1s} are constants corresponding to blade flapping drag. In (3.15), the expression for total hovering thrust $\hat{F}_{hov} = \kappa \sum \Omega_i^2$ and therefore individual rotor thrust of the quadrotor can be given as, $T_{h,i} = \kappa \Omega_i^2$. Then the expression in (3.23) can be written as,

$$D_{Bf,i} = \kappa \Omega_i A_{flap} \frac{V_{H,i}}{R_{ra}}, \quad (3.25)$$

The total drag force D_{Bf} acting on the vehicle from blade flapping effect can be expressed in the following lumped parameter form,

$$D_{Bf} = \sum D_{Bf,i} = K_{D,1} \sum \Omega_i V_H, \quad (3.26)$$

where $K_{D,1}$ is a constant parameter.

Induced drag:

In blade flapping it is assumed that the blades are flexible and thereby counters the imbalance in the lift force. However, if the blades are considered to be stiff or even semi-rigid the advancing blade will generate more lift than the retreating blade and such instantaneous lift will also produce a proportional instantaneous induced drag. The rotor blade on the retreating side experiences less induced drag than the blade on the advancing side during forward flight. Hence, the net instantaneous induced drag experienced by the rotors will directly oppose the apparent wind. This induced drag acting on the vehicle which is proportional to the apparent wind velocity can be given as [9],

$$D_{Id} = \sum D_{Id,i} = K_{D,2} V_H, \quad (3.27)$$

in which $D_{Id,i}$ represents the induced drag for individual rotor i and $K_{D,2}$ is a lumped constant parameter.

Translational drag:

The air sucked in through the rotors with the velocity component called induced velocity ν_{in} is responsible for this drag. In forward flight, the direction of the apparent wind or relative wind velocity is redirected downwards due to the induced flow through the rotors. Such a down-washing of the airflow causes the angle of attack α between the chord line and relative wind flow to shrink. The compensation for the induced flow downwash results in induced lift by increasing the angle of attack. When the rotor blade induces more lift there is also a proportionally induced drag. This effect of drag from induced flow is termed as momentum drag or translational drag. The model for this drag effect as expected would have the component of induced flow and rotor speed in the $x-y$ plane. The expression for translational drag of rotor i at high speed is given by [44],

$$D_{Td,i} = K_T (w_i - \nu_{in,i})^4 V_{H,i}, \quad (3.28)$$

where K_T is a constant, w_i and $\nu_{in,i}$ represent the z -direction velocity and induced velocity of rotor i , respectively. Now using Assumption 3.2.1, the total translational drag D_{Td} acting on the drone can be written in the lumped form using,

$$D_{Td} = \sum D_{Td,i} = K_{D,3} (w - \nu_{in})^4 V_H, \quad (3.29)$$

in which $K_{D,3}$ is the lumped constant for the total translational drag D_{Td} . For the identification model, the expression of the translational drag of rotor i for low speed given by, $D_{Td,i} = K_T V_{H,i}$ is not taken into consideration.

Profile and parasitic drag:

The frictional resistance offered by the rotor blades of the quadrotor when moving through air

causes profile drag [44]. The angle of attack has very little to no effect on this drag force but increases moderately in a linear manner with velocity. However, at very high speed the drag force varies quadratically with increasing velocity. The expression for profile drag D_{Pd} acting on the vehicle is given by,

$$D_{Prd} = \sum D_{Pd,i} = K_{D,4}V_H, \quad (3.30)$$

where $D_{Pd,i}$ is the profile drag for rotor i and $K_{D,4}$ is the lumped constant parameter. The parasitic drag on the other hand is caused by the non-lifting components of the quadrotor such as the outdoor hull, fuselage, motors, rotor hub and landing gear. This drag varies quadratically with velocity and the expression for the quadrotor in the $x-y$ plane is given as [44],

$$D_{Pd} = K_{D,5}V_H|V_H|, \quad (3.31)$$

in which $K_{D,5}$ is the constant parameter. The variation of all the considered drag forces for the quadrotor with respect to body velocity ν is shown in Figure 3.5.

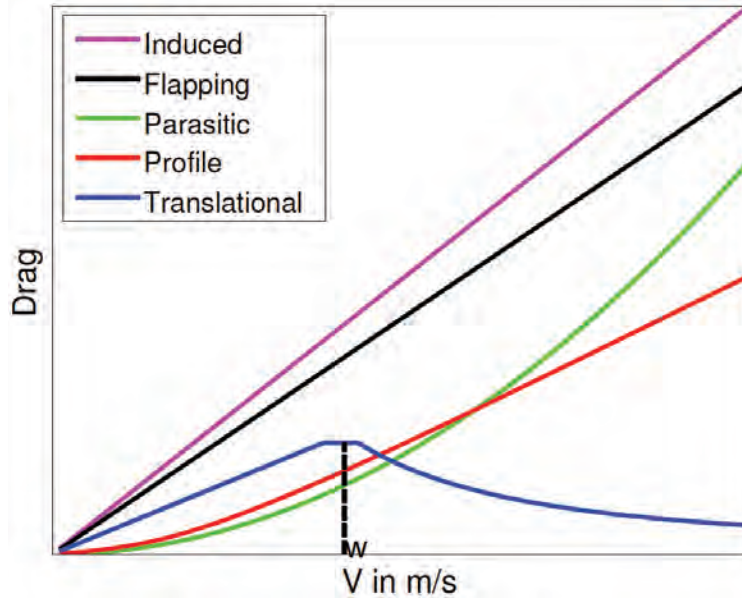


Figure 3.5: Variation of different drag forces with respect to body-fixed velocity ν [44].

From Figure 3.5, it is clear that blade flapping and induced drag are the most dominant drag forces acting on the drone. The translational drag is the most important damping force after these two and has a different behaviour at low and high speed of the quadrotor.

Using (3.26), (3.27), (3.29), (3.30) and (3.31), the total drag forces acting on the $x-y$ plane of the quadrotor can be expressed as,

$$\begin{aligned} \hat{F}_{a,xy} &= D_{Bf} + D_{Id} + D_{Td} + D_{Prd} + D_{Pd} \\ &= K_{D,1} \sum \Omega_i V_H + K_{D,2} V_H + K_{D,3} (w - v_{in})^4 V_H + K_{D,4} V_H + K_{D,5} V_H |V_H| \end{aligned} \quad (3.32)$$

Here the terms with constant $K_{D,2}$ and $K_{D,4}$ can be represented together as constant K_D and hence (3.32) becomes,

$$\hat{F}_{a,xy} = K_{D,1} \sum \Omega_i V_H + K_D V_H + K_{D,3} (w - \nu_{in})^4 V_H + K_{D,5} V_H |V_H| \quad (3.33)$$

The above expression gives an approach to define the model set for aerodynamic force in x -direction by forming polynomial terms of the variables ν and $\sum \Omega_i$. The model predictor terms for model set $\hat{F}_{a,x_{set}}$ is then given by,

$$\begin{aligned} \hat{F}_{a,x_{set}} = & \Theta_0 + \Theta_1 u \sum \Omega_i + \Theta_2 v \sum \Omega_i + \Theta_3 w \sum \Omega_i + \Theta_4 u + \Theta_5 w + \Theta_6 uw \sum \Omega_i + \Theta_7 uw^2 \sum \Omega_i \\ & + \Theta_8 u|u| + \Theta_9 u|v| + \Theta_{10} u|w| + \Theta_{11} w|v| \end{aligned} \quad (3.34)$$

in which Θ_i for $i = 0, 1, \dots, 11$, are the unknown free parameters with Θ_0 being the bias term. In the above expression, the aerodynamic force in x -direction also contains the velocity terms v and w of the $y - z$ plane since the identification experiment with 3D fast trajectory (given in (3.20)) is conducted to capture the drag effects of simultaneous excitation of the horizontal and vertical components. The reasoning for choosing the polynomial terms in set $\hat{F}_{a,x_{set}}$ to model the drag effects are explained through following points:

- The terms $u \sum \Omega_i$, $v \sum \Omega_i$ and $w \sum \Omega_i$ together represents blade flapping drag force D_{Bf} partially. These terms also partly represent the effect of translational drag D_{Td} . The mutual interaction of the rotors and the quadrotor fuselage could also be represented with these terms [31].
- The fifth and sixth predictor term in (3.34) given by u and w represent the effect of induced drag D_{Id} and profile drag D_{Prd} .
- $uw \sum \Omega_i$ and $uw^2 \sum \Omega_i$ represent the effect of translational drag D_{Td} and also the previously mentioned interaction of the rotors and fuselage..
- Furthermore, since the resultant velocity V of the quadrotor in the identification experiment has a component in x, y and z -direction simultaneously during flight, the parasitic drag D_{Pd} will contain terms such as $u|u|$, $u|v|$, $u|w|$ and $|w|v$ in the model set for $F_{a,x}$.

The model selection algorithm from Section 3.1 is applied with $\epsilon_{crit} = 100$ to determine a suitable model for $\hat{F}_{a,x}$ with limited model terms. The output model $\hat{F}_{a,x}$ is selected from the model set using the flight dataset of 3D fast circular maneuver. The chosen output model along with the bias term is given by,

$$\hat{F}_{a,x} = \hat{\theta}_6 + \hat{\theta}_7 u|u| + \hat{\theta}_8 w|v| + \hat{\theta}_9 u \sum \Omega_i + \hat{\theta}_{10} u|w| \quad (3.35)$$

where the parameters $\hat{\theta}_i$ with $i = 6, \dots, 10$, are estimated using the original least squares and are given in Table 3.2.

| Model Predictor | Parameter ($\hat{\theta}$) | Estimated Value | Units |
|-------------------|------------------------------|-----------------------|---|
| $u w $ | $\hat{\theta}_{10}$ | $-1.92 \cdot 10^{-1}$ | Nm^{-2}s^2 |
| $u \sum \Omega_i$ | $\hat{\theta}_9$ | $-6.19 \cdot 10^{-5}$ | $\text{N}(\text{m}\cdot\text{rad})^{-1} \text{s}^2$ |
| $w v $ | $\hat{\theta}_8$ | $1.19 \cdot 10^{-1}$ | Nm^{-2}s^2 |
| $u u $ | $\hat{\theta}_7$ | $-2.90 \cdot 10^{-2}$ | Nm^{-2}s^2 |
| 1 | $\hat{\theta}_6$ | $1.91 \cdot 10^{-1}$ | - |
| NMSE fit | | 88.46 % | |

Table 3.2: Parameters estimates obtained for x -direction drag force model $\hat{F}_{a,x}$ (sorted from most to least relevant).

As seen in Table 3.2, the model predictors obtained for $\hat{F}_{a,x}$ contain most terms that represent the parasitic drag force D_{Pd} . This means the aerodynamic resistance in the x -direction is mostly caused by drag from components of the quadrotor such as outdoor hull, motors and landing gear. The presence of the term $u \sum \omega_i$ in the selected model indicates that the horizontal component of the blade flapping effect D_{Bf} also plays a significant role.

For performing the validation fit test, as a benchmark for comparison the simple x -direction damping force model $F_{D,x}$ given in the work of van den Eijnden [32] is used, which is expressed as,

$$F_{D,x} = -\text{sign}(u) \frac{1}{2} \rho_a c_x u \circ u \quad (3.36)$$

where $c_x = 2.5$ represents the damping coefficient and the density of air is taken as, $\rho_a = 1.2 \text{ kg/m}^3$. Figure 3.6 illustrates the fit results of the simple damping force model $F_{D,x}$ and the estimated model $\hat{F}_{a,x}$ on the validation dataset of aerodynamic force $F_{a,x}$.

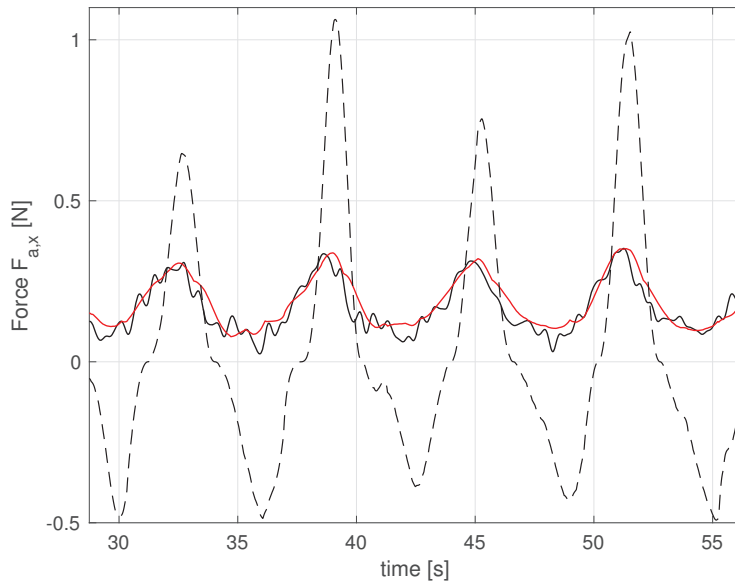


Figure 3.6: Validation fit results on the measurement $F_{a,x}$ (black) with simple damping model $F_{D,x}$ (dashed) and identified aerodynamic model $\hat{F}_{a,x}$ (red) of NMSE fit - 80.85%.

As observed in Figure 3.6, the simple damping force $F_{D,x}$ modeled by [32] overestimates the magnitude of the aerodynamic force and also lags behind in phase with the measurement $F_{a,x}$. The identified aerodynamic model $\hat{F}_{a,x}$ has a NMSE fit of about 80.85% on the measurement. The magnitude and phase of the identified model $\hat{F}_{a,x}$ predicts better in comparison to the damping force model $F_{D,x}$.

The model set for aerodynamic force in y -direction has a similar structure to the one given in (3.34) and is expressed as,

$$\begin{aligned} \hat{F}_{a,y_{set}} = & \Theta_0 + \Theta_1 v \sum \Omega_i + \Theta_2 u \sum \Omega_i + \Theta_3 w \sum \Omega_i + \Theta_4 v + \Theta_5 w + \Theta_6 vw \sum \Omega_i + \Theta_7 vw^2 \sum \Omega_i \\ & + \Theta_8 v|v| + \Theta_9 v|u| + \Theta_{10} v|w| + \Theta_{11} w|u| \end{aligned} \quad (3.37)$$

By model selection with same critical value $\epsilon_{crit} = 100$, the reduced selected model (including term for bias) for aerodynamic force in y -direction is given by,

$$\hat{F}_{a,y} = \hat{\theta}_{11} + \hat{\theta}_{12} v|v| + \hat{\theta}_{13} vw \sum \Omega_i + \hat{\theta}_{14} u \sum \Omega_i + \hat{\theta}_{15} v \sum \Omega_i, \quad (3.38)$$

in which the parameters $\hat{\theta}_i$ with $i = 11, \dots, 15$, are estimated using least squares and the estimates are given in Table 3.3.

| Model Predictor | Parameter ($\hat{\theta}$) | Estimated Value | Units |
|--------------------|------------------------------|-----------------------|---|
| $v \sum \Omega_i$ | $\hat{\theta}_{15}$ | $-1.51 \cdot 10^{-4}$ | $\text{N}(\text{m} \cdot \text{rad})^{-1} \text{s}^2$ |
| $u \sum \Omega_i$ | $\hat{\theta}_{14}$ | $-4.58 \cdot 10^{-5}$ | $\text{N}(\text{m} \cdot \text{rad})^{-1} \text{s}^2$ |
| $vw \sum \Omega_i$ | $\hat{\theta}_{13}$ | $5.14 \cdot 10^{-5}$ | $\text{N}(\text{m}^2 \cdot \text{rad})^{-1} \text{s}^3$ |
| $v v $ | $\hat{\theta}_{12}$ | $7.37 \cdot 10^{-2}$ | $\text{Nm}^{-2} \text{s}^2$ |
| 1 | $\hat{\theta}_{11}$ | $-3.2 \cdot 10^{-2}$ | - |
| NMSE fit | | 82.33 % | |

Table 3.3: Parameters obtained from the estimation dataset for y -direction drag force model $\hat{F}_{a,y}$ (sorted from most to least relevant).

In the Table 3.3 it is noticed that the terms represented by $v \sum \Omega_i$ and $u \sum \Omega_i$ are the most relevant predictors for the model, which could indicate the effect of blade flapping, . After these two model predictors, the term $vw \sum \Omega_i$ denoting partly the effect of translational drag D_{Td} and other complex interactions seems significant for the selected model. Lastly, the parasitic drag term $v|v|$ seem to contribute as well to the drag force model $\hat{F}_{a,y}$

It is observed that the terms of parasitic drag D_{Pd} have only a little role in describing the aerodynamic force $F_{a,y}$ due to the interaction with the quadrotor fuselage in y -direction. During identification it was determined that the inclusion of more parasitic drag terms lead to high variance in the estimated parameters for different datasets. In the work of [36] it is mentioned that the aerodynamic force in the direction projected to large area of the fuselage have quadratically varying parameters. This is expected to be the cause of varying estimated parameters in the identification. It is also to be noted that no similarity in the obtained parameters can be seen for drag force models $\hat{F}_{a,x}$ and $\hat{F}_{a,y}$ as the choice of model terms and the projected area in the x and y -direction

of quadrotor are different. Furthermore, reasoning for the positive values of parameter estimates in $\hat{F}_{a,x}$ and $\hat{F}_{a,y}$ is unknown and needs to be investigated in future work. Again for comparison, we use the y -direction damping force model $F_{D,y}$ used in the work of [32], given by,

$$F_{D,y} = -\text{sign}(v) \frac{1}{2} \rho_a c_y v \circ v \quad (3.39)$$

where $c_y = 1.3$ is the damping coefficient. Figure 3.7 shows the validation fit results of the damping force model $F_{D,y}$ and identified aerodynamic model $\hat{F}_{a,y}$ on the measurement $F_{a,y}$ from 3D circular maneuver trajectory. Here it observed that the model $F_{D,y}$ representing the parasitic drag predicts accurately the magnitude of the y -direction aerodynamic force at some instances and overestimates in other instances which suggest that the y -direction damping force occurs with a combination of different drag forces. The identified model $\hat{F}_{a,y}$ takes into account the combination of these drag forces and actively predicts the aerodynamic force acting in the y -direction of the quadrotor with a 81.9 % validation fit.

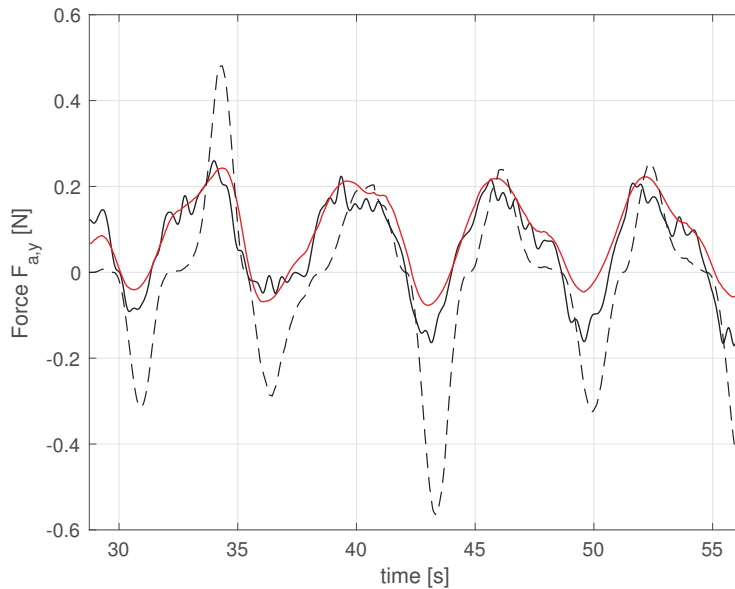


Figure 3.7: Validation fit results on the measurement $F_{a,y}$ (black) with simple damping model $F_{D,y}$ (dashed) and identified aerodynamic model $\hat{F}_{a,y}$ (red) of NMSE fit - 81.9%.

3.4 Roll and Pitch Moment Model

In this section, with the proposed identification method the roll and pitch moment models (\hat{M}_x and \hat{M}_y) are determined. The aerodynamic moments acting on the air-frame of the quadrotor are generally considered to surface from all the drag forces except the parasitic drag (defined in the previous section). In theoretical models, the rotor generated drag forces and their respective offset from the center of gravity is used to model the aerodynamic moment.

However, for our configuration of the quadrotor the moment models are identified from IMU gyroscope measurements. This enables to determine the drag forces that are actually responsible

for the external torque on the quadrotor. It also helps in ascertaining if the aerodynamic drag forces which were identified in the previous section have contribution to external moments as well. However unlike aerodynamic forces, the external aerodynamic moments are much more difficult to approximate with linear-in-parameters models.

To model the roll and pitch moment models we consider the following torque inputs given by,

$$\begin{aligned}\tau_1 &= \kappa l V_p \\ \tau_2 &= \kappa l V_q\end{aligned}\quad (3.40)$$

where τ_1 and τ_2 are the control outputs used to control the roll and pitch motion of the quadrotor, respectively, κ is the hovering thrust coefficient determined in Section 3.2 and l is the distance of the rotor centers from the center of gravity. Also, V_p and V_q represent the rotor speed combination of each rotor i given by,

$$V_p = \Omega_1^2 - \Omega_2^2 - \Omega_3^2 + \Omega_4^2, \quad V_q = -\Omega_1^2 - \Omega_2^2 + \Omega_3^2 + \Omega_4^2 \quad (3.41)$$

The total external roll moment \hat{M}_x acting on the quadrotor can be represented as follows,

$$\hat{M}_x = \tau_1 + \hat{M}_{a,x} \quad (3.42)$$

in which the aerodynamic roll moment model $\hat{M}_{a,x}$ is determined using model set $\hat{M}_{a,x_{set}}$ which is defined by polynomial predictors formed by ν , ω , V_p and $\sum \Omega_i$. The model set $\hat{M}_{a,x_{set}}$ is expressed as follows,

$$\hat{M}_{a,x_{set}} = \Theta_0 + \Theta_1 \nu \sum \Omega_i + \Theta_2 \nu + \Theta_3 \omega + \Theta_4 \nu \omega \sum \Omega_i + \Theta_5 p + \Theta_6 \nu V_p + \Theta_7 \nu^2 V_p + \Theta_8 \omega^2 V_p \quad (3.43)$$

The above model set is selected based on the following reasoning:

- The second to fifth terms in (3.43) resembles the model set $\hat{F}_{a,y_{set}}$ in (3.37) since the rolling motion of the quadrotor results in linear velocity components in y and z -direction. Therefore, the rolling motion of the vehicle is damped and dependent on velocity terms ν and ω . The complex interaction of the other velocity terms from set $\hat{F}_{a,y_{set}}$ are excluded in set $\hat{M}_{a,x_{set}}$ due to the difficulty of modeling aerodynamic moments.
- The term representing the roll rate p in $\hat{M}_{a,x_{set}}$ is used to take into account the rotational damping from rolling maneuvers.
- The coefficient of the roll control output τ_1 is given by κl as represented in (3.40) but it is determined that this coefficient varies when the quadrotor rolls to fly sideways. Hence, the terms νV_p , $\nu^2 V_p$ and $\omega^2 V_p$ are used to take into account this mismatch in the roll control. The coupling of the rotor speed combination V_p with the velocity terms ensures that this effect becomes negligible when the quadrotor is hovering.

Using the IMU gyroscope outputs, the net internal roll moment M_x is calculated for the 3D circular trajectory (given in (3.20)) flight dataset. The roll aerodynamic moment measurement $M_{a,x}$ is then obtained by $M_{a,x} = M_x - \tau_1$, which is used for applying the model selection criterion with $\epsilon_{crit} = 300$. A larger value of ϵ_{crit} is chosen for roll moment model selection since aerodynamic moments have very little influence on damping the quadrotor motion at low airspeed ($V \leq 2$ m/s). The selected model $\hat{M}_{a,x}$ is given as follows,

$$\hat{M}_{a,x} = \hat{\theta}_{16} + \hat{\theta}_{17} \nu^2 V_p + \hat{\theta}_{18} \omega^2 V_p + \hat{\theta}_{19} \nu \quad (3.44)$$

The parameters of the output model $\hat{M}_{a,x}$ are estimated using least squares and are provided in Table 3.4.

| Model Predictor | Parameter ($\hat{\theta}$) | Estimated Value | Units |
|-----------------|------------------------------|-----------------------|--|
| v | $\hat{\theta}_{19}$ | $1.82 \cdot 10^{-2}$ | Ns |
| $w^2 V_p$ | $\hat{\theta}_{18}$ | $-2.13 \cdot 10^{-6}$ | $\text{N}(\text{m}\cdot\text{rad}^2)^{-1}\text{s}^4$ |
| $v^2 V_p$ | $\hat{\theta}_{17}$ | $-2.06 \cdot 10^{-7}$ | $\text{N}(\text{m}\cdot\text{rad}^2)^{-1}\text{s}^4$ |
| 1 | $\hat{\theta}_{16}$ | $1.14 \cdot 10^{-3}$ | - |
| NMSE fit | | 76.99 % | |

Table 3.4: Estimated parameters for selected model $\hat{M}_{a,x}$ (sorted from most to least relevant).

Similarly, the model set $M_{a,y_{set}}$ is defined along the same lines as the model structure given in (3.43) and is expressed as,

$$\hat{M}_{a,y_{set}} = \Theta_0 + \Theta_1 u \sum \Omega_i + \Theta_2 u + \Theta_3 w + \Theta_4 uw \sum \Omega_i + \Theta_5 q + \Theta_6 u V_q + \Theta_7 u^2 V_q + \Theta_8 w^2 V_q \quad (3.45)$$

The measurement $M_{a,y} = M_y - \tau_2$, from the gyroscope outputs of the previously used flight dataset is used for model selection. The obtained output model $\hat{M}_{a,y}$ using the previous cut-off value for term selection i.e., $\epsilon_{crit} = 300$ is given by,

$$\hat{M}_{a,y} = \hat{\theta}_{20} + \hat{\theta}_{21} u + \hat{\theta}_{22} u^2 V_q + \hat{\theta}_{23} w^2 V_q, \quad (3.46)$$

where the parameter estimates θ_i for $i = 20, \dots, 23$, are shown in Table 3.5.

| Model Predictor | Parameter ($\hat{\theta}$) | Estimated Value | Units |
|-----------------|------------------------------|------------------------|--|
| $w^2 V_q$ | $\hat{\theta}_{23}$ | $-2.185 \cdot 10^{-6}$ | $\text{N}(\text{m}\cdot\text{rad}^2)^{-1}\text{s}^4$ |
| $u^2 V_q$ | $\hat{\theta}_{22}$ | $-9.94 \cdot 10^{-7}$ | $\text{N}(\text{m}\cdot\text{rad}^2)^{-1}\text{s}^4$ |
| u | $\hat{\theta}_{21}$ | $-1.51 \cdot 10^{-2}$ | Ns |
| 1 | $\hat{\theta}_{20}$ | $-4.4 \cdot 10^{-3}$ | - |
| NMSE fit | | 91.35 % | |

Table 3.5: Moment model $\hat{M}_{a,y}$ estimated parameters (sorted from most to least relevant).

The external aerodynamic moments affecting the roll and pitch motion have similar choice of terms, as seen in (3.44) and (3.46) for $\hat{M}_{a,x}$ and $\hat{M}_{a,y}$, respectively. In both moment models, the predictor terms involving rotor speed combination V_p and V_q are considered to be significant. This implies that the coefficients of the torque inputs τ_1 and τ_2 given in (3.40) vary when the quadrotor performs flight maneuvers. Also, the horizontal velocity terms v and u in models $\hat{M}_{a,x}$ and $\hat{M}_{a,y}$, respectively, indicate that the quadrotor experiences an aerodynamic moment due to the drag forces in $x - y$ plane. No similar patterns in the parameter estimates can be observed for roll and pitch moment models as the projected area in x and y -direction of the quadrotor is different.

The disturbance moment from gyroscopic effect of the rotors $\hat{M}_{gyro} = [\hat{M}_{gyro,x}, \hat{M}_{gyro,y}]^T$, affecting the roll and pitch motion is given by [44],

$$\hat{M}_{gyro} = -J_r \sum_{i=1}^4 (-1)^{i+1} S(\omega) b_3 \Omega_i, \quad (3.47)$$

where J_r represents the moment of inertia of the rotor. The estimation of this disturbance moment showed that it had very little significance on the net roll and pitch moment of the quadrotor. This is suspected to be caused by the counter rotating rotors of the quadrotor which makes the disturbance torque \hat{M}_{gyro} virtually negligible and thereby are excluded from the roll and pitch moment models.

The validation fit results of the estimated of roll external moment model $\hat{M}_x = \tau_1 + \hat{M}_{a,x}$ on measurement M_x is shown in Figures 3.8. For comparison, the hovering roll input model τ_1 is plotted against the measurement M_x as well. Similarly in Figure 3.9, the fit of the identified pitch moment model $\hat{M}_y = \tau_2 + \hat{M}_{a,y}$ and the hovering pitch model τ_2 on the measurement M_y is illustrated.

In figures 3.8 and 3.9 it is observed that the magnitude of the moment measurements (M_x and M_y) are much lower than the identified models ($\hat{M}_{a,x}$ and $\hat{M}_{a,y}$) and the simple hovering models (τ_1 and τ_2). However, the magnitude of the identified models are more damped and closer to the validation dataset than the initially considered hovering roll and pitch models. The poor validation fit of the identified moment models is expected, since linear-in-parameters models are insufficient to capture the aerodynamic moments acting on the quadrotors [36]. In Section 3.6, the variation of parameters with respect to speed in moment models is briefly discussed to explain this complex behaviour. In the current state of the quadrotor it is difficult to perform aggressive angular maneuvers for large magnitude of moment measurements. This is also suspected to be the reason of the unsatisfactory fit results from the poor parameter estimates.

Furthermore, during experiments the protective outdoor hull was attached to the quadrotor. This loosely attached hull results in unsteady pitch and roll motions of the quadrotor which in turn leads to constantly fluctuating aerodynamic moments acting on the quadrotor.

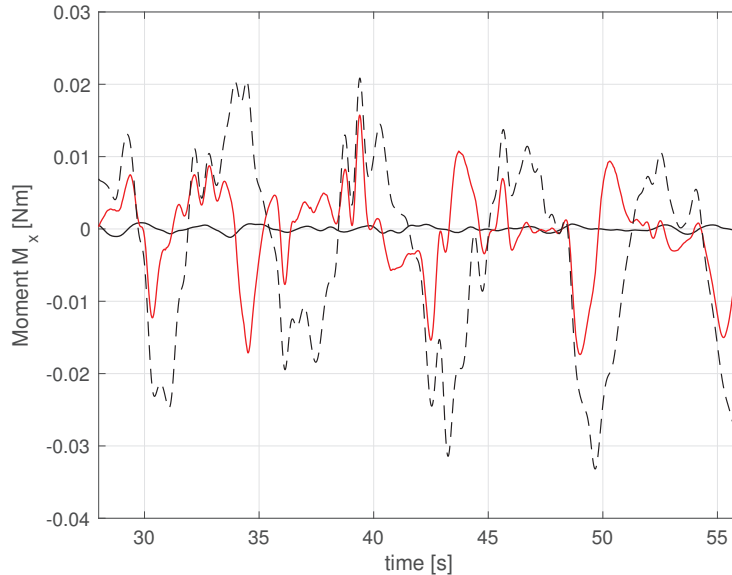


Figure 3.8: Validation fit results on the measurement M_x (black) with hovering roll model τ_1 (dashed) and identified roll moment model \hat{M}_x (red).

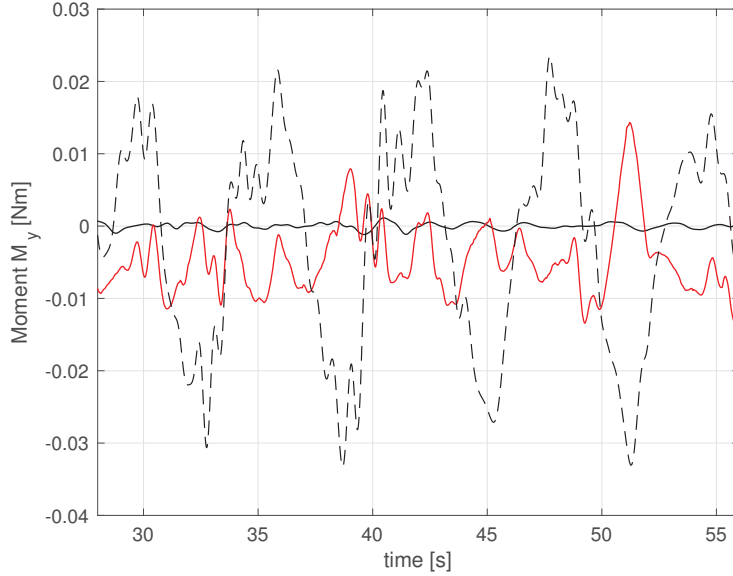


Figure 3.9: Validation fit results on the measurement M_y (black) with hovering pitch model τ_2 (dashed) and identified pitch moment model \hat{M}_y (red).

3.5 Yaw Moment Model

This section determines the model for yaw moment during hovering and other aggressive flight maneuvers. The net external yaw moment acting on the vehicle can be expressed as,

$$\begin{aligned}\hat{M}_z &= \tau_3 + \hat{M}_d e_3 + \hat{M}_{a,z} \\ &= dV_r + \hat{M}_{rot,z} + \hat{M}_{a,z},\end{aligned}\quad (3.48)$$

where d is the drag coefficient and $V_r = \Omega_1^2 - \Omega_2^2 + \Omega_3^2 - \Omega_4^2$, is the rotor speed combination defined for yaw input torque. The disturbance moment resulting from rotor inertia $\hat{M}_{rot,z}$ is given as,

$$\hat{M}_{rot,z} = J_r(-\dot{\Omega}_1 + \dot{\Omega}_2 - \dot{\Omega}_3 + \dot{\Omega}_4) \quad (3.49)$$

To estimate the model of yaw moment during hovering, the flight data for the quadrotor should be obtained by conducting experiments to perform yaw motions while hovering at a stationary point. This results in flight datasets where body-fixed velocity, $\nu = 0$ and angular rates for roll and pitch becomes negligible as well. The model for yaw moment during hovering and can be given by,

$$\hat{M}_{hov,z} = dV_r + J_r(-\dot{\Omega}_1 + \dot{\Omega}_2 - \dot{\Omega}_3 + \dot{\Omega}_4) + \gamma r, \quad (3.50)$$

in which the term γr represent the effect of rotational damping for yaw rate r . The flight dataset for hovering yaw moment model $\hat{M}_{hov,z}$ is obtained using the toolbox designed in the work of Marx [45]. The graphical user interface of the toolbox enables to perform manual yaw maneuvers during hovering.

The estimation datasets are then used to determine the parameters $[d, J_r, \gamma]^T$ of the hovering yaw moment model $\hat{M}_{hov,z}$ which is given in Table 3.6. The table shows that the parameter γ for the

rotational damping is negative which is expected.

| Parameters | Estimated value | Units |
|------------|-----------------------|-------------------------------------|
| d | $5.14 \cdot 10^{-9}$ | Nm·rad ⁻² s ² |
| J_r | $2.12 \cdot 10^{-6}$ | Nm·rad ⁻¹ s ² |
| γ | $-2.02 \cdot 10^{-3}$ | Nm·rad ⁻¹ s |

Table 3.6: Estimated parameters of hovering yaw moment model $\hat{M}_{hov,z}$

The net yaw moment for other cases such as forward flights as given in (3.48) can be written as follows,

$$\hat{M}_z = \hat{M}_{hov,z} + \hat{M}_{a,z}, \quad (3.51)$$

in which $\hat{M}_{a,z}$ accounts for the other aerodynamic effects when the quadrotor performs other maneuvers and the model set $\hat{M}_{a,z_{set}}$ is hence given by,

$$\hat{M}_{a,z_{set}} = \Theta_0 + \Theta_1 v \sum \Omega_i + \Theta_2 u \sum \Omega_i + \Theta_3 v + \Theta_4 u + \Theta_5 v V_r + \Theta_6 v^2 V_r + \Theta_6 u V_r \quad (3.52)$$

where the first few terms resemble the model predictors for the drag forces in x - y plane. The other terms, such as vV_r , v^2V_r and V_r accounts for the mismatch in yaw torque input in forward flights. The 3D circular trajectory flight dataset is used again for the model selection from set $\hat{M}_{a,z_{set}}$. The output measurement M_z obtained from the IMU gyroscope and the estimated hovering moment model $\hat{M}_{hov,z}$ is used to isolate the yaw aerodynamic measurement using, $M_{a,z} = M_z - \hat{M}_{hov,z}$. The chosen output model $\hat{M}_{a,z}$ form the model selection algorithm with $\epsilon_{crit} = 300$ is given by,

$$\hat{M}_{a,z} = \hat{\theta}_{24} + \hat{\theta}_{25}u + \hat{\theta}_{25}v \quad (3.53)$$

The above output model has smaller number of terms as the term representing the rotational damping effect given by γr is already included in the hovering yaw moment model $\hat{M}_{hov,z}$. Therefore, the total aerodynamic yaw moment for the quadrotor is represented by the term γr and the predictors determined in (3.53) for model $\hat{M}_{a,z}$. The estimated parameters for the selected model $\hat{M}_{a,z}$ is given in Table 3.7. The estimation fit for few selected terms is about 44.53 % which can be further increased to about 70 % with inclusion of more model terms.

| Model Predictor | Parameter ($\hat{\theta}$) | Estimated Value | Units |
|-----------------|------------------------------|-----------------------|-------|
| v | $\hat{\theta}_{26}$ | $-1.33 \cdot 10^{-3}$ | Ns |
| u | $\hat{\theta}_{25}$ | $-2.64 \cdot 10^{-4}$ | Ns |
| 1 | $\hat{\theta}_{24}$ | $-3.9 \cdot 10^{-4}$ | - |
| NMSE fit | | 44.53 % | |

Table 3.7: Estimated parameters for moment model $\hat{M}_{a,z}$ (sorted from most to least relevant).

The fit of the identified net external yaw moment model $\hat{M}_z = \hat{M}_{a,z} + \hat{M}_{hov,z}$ against the validation dataset is given in Figure 3.10. Compared to the estimation fit results, the validation fit in Figure 3.10 is good for the estimated yaw moment model \hat{M}_z . Unlike the roll and pitch moments, the yaw

moment acting on the drone at low speed ($V \leq 2\text{m/s}$) is relatively easier to be approximated with linear-in-parameters models. Also, the yaw motion of the quadrotor is much more steady than the roll and pitch motions. Therefore, the measurement of yaw moment M_z has a good correlation with the model predictors.

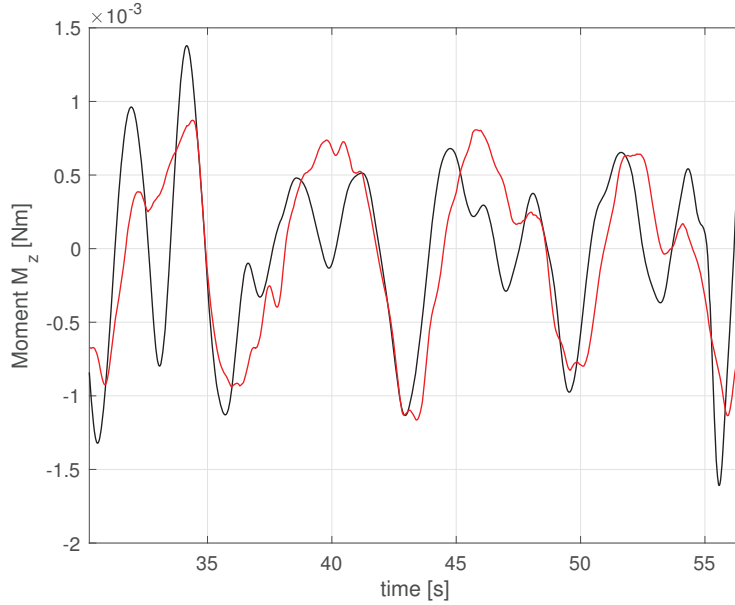


Figure 3.10: Validation fit results on the measurement M_z (black) with identified yaw moment model \hat{M}_z (red) of NMSE fit 43.30 %.

The estimation and validation fit of the yaw moment model \hat{M}_z can be increased by including more model predictor terms. However, unlike the aerodynamic force models, the yaw aerodynamic moment model $\hat{M}_{a,z}$ requires more than ten predictor terms for a significant increase in fit. This is because when more model predictors other than the ones given in (3.52) are included to the model, they contribute very little to increase the fit on the measurement. The yaw moment model with more model predictors is detailed in Appendix E. The increase in the model terms will indeed result in improved estimation fit but due to the increased model complexity, the validation fit will be much lower than the estimation fit. With the increase of model complexity there will always be increase in the variance of the parameters for different measurement sets. Therefore, a reduced validation fit can be expected for the complex yaw moment model with large number of terms.

3.6 Comments on Identified Models

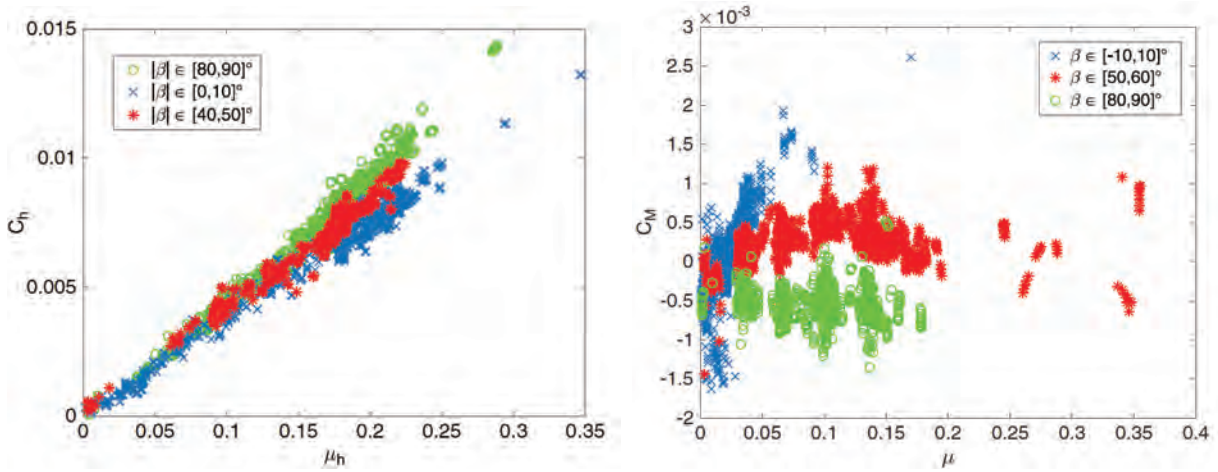
In identification it is a common approach to study the variation in estimated parameters of the chosen model set by methods such as Monte Carlo simulations. The limited datasets available for identification makes it difficult to study how the coefficients of the selected model structure changes for different flight conditions. Fortunately, the recent work of Sun and Visser in [36] has studied this variation of coefficients in force and moment models with respect to the air speed. It was determined that angle of attack α and side slip angle β are the two deciding factors that influence

this change, which are given by,

$$\begin{aligned}\alpha &= \arcsin(w/V) \\ \beta &= \arcsin\left(v/\sqrt{u^2 + v^2}\right)\end{aligned}\quad (3.54)$$

In Figure 3.11a the variation of the horizontal force coefficient $C_h = \sqrt{C_x^2 + C_y^2}$ with respect to the advance ratio $\mu_h = \sqrt{\mu_x^2 + \mu_y^2}$ in different side slip angle β intervals is illustrated. The expressions for these dimensionless parameters can be seen in the work of [36].

Similarly, Figure 3.11b shows the variation of pitch moment coefficient C_m with respect to advance ratio $\mu = \sqrt{\mu_x^2 + \mu_y^2 + \mu_z^2}$ with constant range of angle of attack α and different intervals of β .



(a) Horizontal force coefficient C_h vs advance ratio μ_h . (b) Pitch moment coefficient C_m vs advance ratio μ .

Figure 3.11: Variation of horizontal force and pitch moment coefficients in different intervals of side slip angle β [36].

In Figure 3.11a, it is seen that horizontal force coefficient C_h remains linear with respect to the horizontal speed and varies slightly for the three different intervals β . The work of [36] states that this is due to the slight quadratic variation of aerodynamic force in y -direction. The large exposed area of the quadrotor fuselage in y -direction is suspected to be the cause of this quadratic coefficient behaviour which was mentioned in Section 3.3.

The non-linear behaviour of the pitch moment coefficient C_m with respect to the rotor averaged air speed μ is observed in Figure 3.11b. This can be regarded as one of the reasons for the poor validation fit results of the roll and pitch moment model in Section 3.4.

Figure 3.11 also further affirms the choice of identification using the 3D circular trajectory for the quadrotor to follow as this reference covers a large range α and β . The complex aerodynamic behaviour modeled using this dataset should be valid for a large flight envelope of the quadrotor. Similar plots for coefficient variation of thrust and yaw moment can be seen in [36].

3.7 Concluding Remarks

This chapter is dedicated for the identification of the aerodynamic forces and moments acting on the quadrotor. The identification involves defining grey-box model structures for capturing the aerodynamic effects and selecting most appropriate set of model predictors from the structures based on a model selection algorithm. The Least Angle Regression algorithm with few modifications is used to select the most suitable model terms for the output model. Model selection plays a significant role as it does not only select the model terms based on the correlation with output data. The implemented selection criterion considers choosing the appropriate model terms based on the terms already existing in the model. The decisive algorithm also determines if the any term should be dropped out of the model in order to add another more correlated model term. This approach yields models with least number of terms and also a good estimation fit. Another important aspect of the identification procedure is tailoring specific flight experiments. In the case of identification of the hovering thrust model, the quadrotor should hover motionless such that all the linear and angular velocities become negligible. Similarly for the hovering yaw moment model, the quadrotor needs to hover and perform yaw motions. For the identification of all the other aerodynamic effects which are motion dependent, the quadrotor is made to follow a 3D circular reference trajectory. The models identified with this flight data takes into consideration the complex interactions of horizontal and vertical motions of the quadrotor. Also, a large range of angle of attack and side slip angle is covered in the datasets for this maneuver. The identified net external forces \hat{F}_{ext} acting on the quadrotor can hence be represented as the sum of forces acting on the drone while hovering, given by f and forces that dependent of the motion of quadrotor which is denoted by \hat{F}_{aero} . The expression for net external forces $\hat{F}_{ext} = [\hat{F}_{a,x}, \hat{F}_{a,y}, \hat{F}_z]^T$ excluding all the considered bias terms is given by,

$$\hat{F}_{ext} = f + \hat{F}_{aero}$$

$$\hat{F}_{ext} = \begin{bmatrix} 0 \\ 0 \\ \kappa \sum \Omega_i^2 \end{bmatrix} + \begin{bmatrix} \hat{\theta}_1 u|u| + \hat{\theta}_2 w|v| + \hat{\theta}_3 u \sum \Omega_i + \hat{\theta}_4 u|w| \\ \hat{\theta}_5 vw \sum \Omega_i + \hat{\theta}_6 v|v| + \hat{\theta}_7 u \sum \Omega_i + \hat{\theta}_8 v \sum \Omega_i \\ \hat{\theta}_9 (v^2 + u^2) + \hat{\theta}_{10} u \sum \Omega_i + \hat{\theta}_{11} v \sum \Omega_i + \hat{\theta}_{12} w \sum \Omega_i \end{bmatrix} \quad (3.55)$$

The above identified model has yielded 12 terms for the total external disturbance forces and the estimation and validation fit results of each identified force model is given in Table 3.8.

| Model | Estimation fit (%) | Validation fit(%) |
|-----------------|--------------------|-------------------|
| \hat{F}_z | 85.86 | 70.53 |
| $\hat{F}_{a,x}$ | 88.46 | 80.85 |
| $\hat{F}_{a,y}$ | 82.33 | 81.9 |

Table 3.8: Estimation and Validation fit results of all the identified external disturbance force models

The net external moments $\hat{M}_{ext} = [\hat{M}_x, \hat{M}_y, \hat{M}_z]^T$ can also be expressed as the sum of the moments during hovering, \hat{M}_{hov} and motion dependent disturbance moment (\hat{M}_{aero}). The term \hat{M}_{hov} is further expressed as the sum of input torques τ and disturbance moment \hat{M}_d resulting from rotor inertia, i.e., $\hat{M}_{hov} = \tau + \hat{M}_d$. The net external moments \hat{M}_{ext} can hence be given as,

$$\hat{M}_{ext} = \tau + \hat{M}_d + \hat{M}_{aero}$$

$$\hat{M}_{ext} = \begin{bmatrix} \kappa l V_p \\ \kappa l V_q \\ d V_r \end{bmatrix} + \begin{bmatrix} 0 \\ 0 \\ J_r(-\dot{\Omega}_1 + \dot{\Omega}_2 - \dot{\Omega}_3 + \dot{\Omega}_4) \end{bmatrix} + \begin{bmatrix} \hat{\theta}_{13} v^2 V_p + \hat{\theta}_{14} w^2 V_p + \hat{\theta}_{15} v \\ \hat{\theta}_{16} u + \hat{\theta}_{17} u^2 V_q + \hat{\theta}_{18} w^2 V_q \\ \hat{\theta}_{19} r + \hat{\theta}_{20} u + \hat{\theta}_{21} v \end{bmatrix} \quad (3.56)$$

In the identified roll and pitch moment models, the validation fit results seemed to be quite unsatisfactory as the roll and pitch motion moment measurements have small magnitudes and are unsteady in nature. The external aerodynamic moments are also found to be difficult to capture with linear-in-parameters models. The yaw moment model however are found to have better validation fit results and also improvement in the fit has also been observed with further increase in model terms.

The important feature of the identified force and moment models is that when the quadrotor is hovering with linear and angular velocity equal to zero, the expressions in (3.55) and (3.56) becomes $\hat{F}_{ext} = f$ and $\hat{M}_{ext} = \hat{M}_{hov}$. The coupling of all the model terms with either the body-fixed velocity ν or the angular velocity ω makes this arrangement possible.

The quadrotor system can be then represented with the rigid body dynamics and the identified aerodynamics ($\hat{F}_{ext}, \hat{M}_{ext}$) as follows,

$$\dot{\rho} = R\nu \quad (3.57a)$$

$$\dot{\nu} = -S(\omega)\nu - gR^T e_3 + \frac{f}{m} e_3 + \frac{\hat{F}_{aero}}{m} \quad (3.57b)$$

$$\dot{R} = RS(\omega) \quad (3.57c)$$

$$J\dot{\omega} = S(J\omega)\omega + \tau + \hat{M}_d + \hat{M}_{aero}, \quad (3.57d)$$

using this extended model, the previously used cascaded controller in the work of [33] is re-designed in Chapter 4.

Chapter 4

Controller Re-design

In this chapter the tracking controller for the quadrotor model with extended dynamics is derived. The stability of the controller is proved along the same lines as in the work of [33]. In Figure 4.1, the block diagram of the control structure is presented. As seen in the figure, the reference trajectory for desired aerodynamic forces given by $F_{r,aero}$ and disturbance moments given by $M_{r,aero}$ and $M_{r,d}$ is generated for the updated controller. This additional reference is required so that the identified disturbance force model \hat{F}_{aero} and disturbance moment models \hat{M}_{aero} and \hat{M}_d acting externally on the quadrotor tracks the disturbance forces and moments of the desired reference trajectory. The control scheme in Figure 4.1 shows a natural cascaded structure where the dynamics of the position subsystem is influenced by the output of the attitude subsystem. Considering the cascaded form and the underactuated characteristics of the system, the desired position dynamics is therefore attained by generating the new attitude reference R^* for the attitude tracking controller.

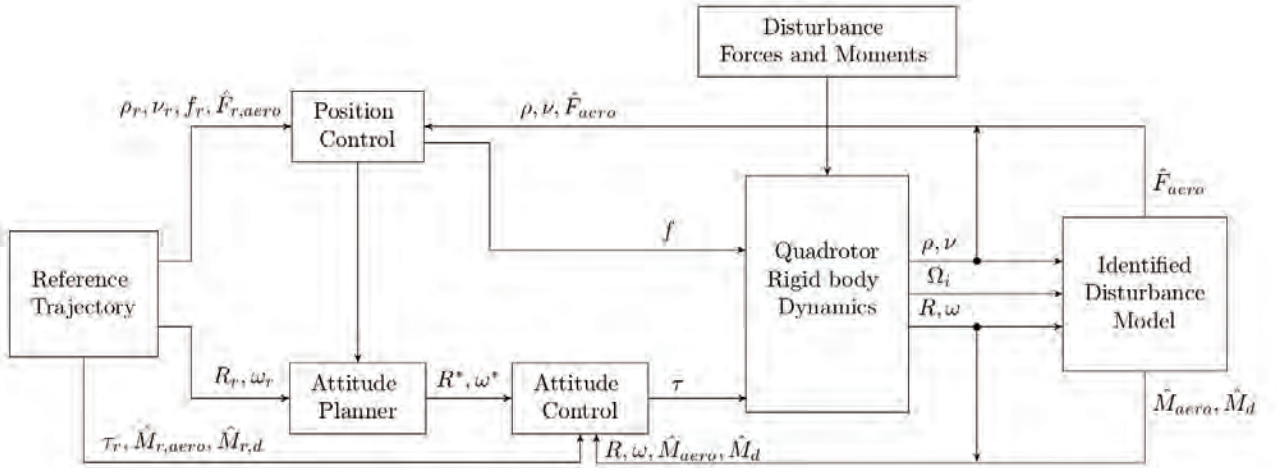


Figure 4.1: Schematic representation of the tracking controller structure using the extended model in (3.57).

In Section 4.1, the definitions and convergence results required to derive the almost global stability of the tracking controller is presented. The tracking problem of the quadrotor is formulated in Section 4.2 with the desired reference trajectory dynamics. Sections 4.3 and 4.4 presents the re-

design of the tracking controllers for the position and attitude subsystems. The stability of resulting cascaded closed-loop system is then analyzed in Section 4.5.

4.1 Preliminaries

This section describes the definitions and stability theorems utilized for re-designing the cascaded controller.

4.1.1 Saturation Function

The nonlinearity resulting from actuator saturation is one of the most common encountered issues in feedback problems. For controlling the quadrotor, this input saturation problem is directly taken into account in the design of the state feedback control law. A saturation vector-function $\sigma(e)$, $\sigma : \mathbb{R}^n \rightarrow \mathbb{R}^n$ defined for vector e_i for $i \in \{1, 2, 3\}$ satisfies the following condition,

$$e^T \sigma(e) > 0, \quad \forall e \neq 0 \quad \text{and} \quad \frac{d\sigma}{de}(0) > 0. \quad (4.1)$$

In addition, the saturation vector-function σ satisfies the bound, $\|\sigma(e)\| \leq M$ for all e . For the controller used in this chapter, a possible candidate that can be used for the saturation vector-function $\sigma(e)$ is given by,

$$\sigma(e) = \frac{e}{\sqrt{1 + e^T e}} \quad (4.2)$$

4.1.2 Stability Definitions and Results

Consider a non-autonomous system given by,

$$\dot{x} = f(t, x) \quad x(t_0) = x_0, \quad (4.3)$$

where $f(t, 0) = 0$, $f : \mathbb{R}^+ \times D \subset \mathbb{R}^n \rightarrow \mathbb{R}^n$ is piecewise continuous on $\mathbb{R}^+ \times D$ and locally Lipschitz in x on $\mathbb{R}^+ \times D$.

To explain the stability definitions for the system in (4.3), following comparison functions are utilized,

Definition 4.1.1 ([46])

- A continuous function $\alpha : [0, a) \rightarrow [0, \infty)$ belongs to class \mathcal{K} if it is strictly increasing and $\alpha(0) \rightarrow 0$. In addition, the function belongs to class \mathcal{K}_∞ if $a = \infty$ and $\alpha(r) \rightarrow \infty$ as $r \rightarrow \infty$.
- A continuous function $\beta : [0, a) \times [0, \infty) \rightarrow [0, \infty)$ is said to belong to class \mathcal{KL} if for each fixed s , the mapping $\beta(r, s)$ is class \mathcal{K} and for each fixed r , the mapping $\beta(r, s)$ is decreasing with respect to s and $\beta(r, s) \rightarrow 0$ as $s \rightarrow \infty$.

Following notions of stability are used to prove the robustness of the proposed controller,

Definition 4.1.2 The equilibrium point $x = 0$ is [46],

- (locally) uniformly asymptotically stable if and only if there exists a function $\beta \in \mathcal{KL}$ and a constant $c > 0$, independent of t_0 such that,

$$\|x(t)\| \leq \beta(\|x(t_0)\|, t - t_0) \quad t \geq t_0 \geq 0, \quad \|x(t_0)\| < c \quad (4.4)$$

- uniformly globally asymptotically stable (UGAS) if the inequality in (4.4) is satisfied for all $x(t_0)$.
- uniformly almost globally asymptotically stable (UaGAS) if it is UGAS, except for all initial conditions in a set of measure zero.
- uniformly locally exponentially stable (ULES)/ uniformly globally exponentially stable (UGES) if it is (locally) uniformly asymptotically stable/uniformly globally asymptotically stable respectively and (4.4) is satisfied with,

$$\beta(r, s) = kre^{\gamma s} \quad k > 0, \gamma > 0. \quad (4.5)$$

Theorem 4.1.1 (Nested Matrosov Theorem [47], Theorem 1): Consider the nonautonomous system,

$$\dot{x} = f(t, x) \quad x(t_0) = x_0 \quad (4.6)$$

with $f(t, 0) = 0$, $f : \mathbb{R}^+ \times \mathbb{R}^n \rightarrow \mathbb{R}^n$ locally bounded, continuous and locally uniformly continuous in t .

Considering there exists j differential functions $V_i : \mathbb{R}^+ \times \mathbb{R}^n \rightarrow \mathbb{R}$ bounded in t and continuous functions $Y_i : \mathbb{R}^n \rightarrow \mathbb{R}$ for $i \in \{1, 2, \dots, j\}$ such that,

- function V_1 is positive definite,
- $\dot{V}_i(t, x) \leq Y_i(x)$ for all $i \in \{1, 2, \dots, j\}$,
- $Y_i(x) = 0$ for $i \in \{1, 2, \dots, k-1\}$ implies that $Y_k(x) \leq 0$ for all $k \in \{1, 2, \dots, j\}$,
- $Y_i(x) = 0$ for all $i \in \{1, 2, \dots, j\}$ implies that $x = 0$,

then the origin $x = 0$ of (4.6) is uniformly globally asymptotically stable (UGAS).

Theorem 4.1.2 ([33], Theorem 4): Consider the system,

$$\dot{R} = RS(\omega) \quad (4.7a)$$

$$J\dot{\omega} = -K_\omega\omega + K_R \sum_{i=1}^3 k_i(e_i \times R^T e_i), \quad (4.7b)$$

in which $R \in \mathcal{SO}(3) = \{R \in \mathbb{R}^{3 \times 3} \mid R^T R = I, \det R = 1\}$, $\omega \in \mathbb{R}^3$, $J = J^T > 0$.

The equilibrium point $(I, 0)$ of (4.7) is uniformly locally exponentially stable (ULES) and uniformly almost global exponentially stable (UaGAS) if $K_\omega = K_\omega^T > 0$, $K_R = K_R^T > 0$ and the values of $k_i > 0$ are chosen distinctly. That is, let the four equilibria of R given by,

$$\mathcal{E}_c = \{I, \text{diag}(1, -1, -1), \text{diag}(-1, 1, -1), \text{diag}(-1, -1, 1)\} \quad (4.8)$$

Then R and ω converge to \mathcal{E}_c and zero, respectively. The undesired equilibria $(R, 0)$ of (4.7), where $R \in \mathcal{E}_c \setminus \{I\}$ are unstable and the set of all initial conditions converging to the equilibrium $(R, 0)$, where $R \in \mathcal{E}_c \setminus \{I\}$ form a lower dimensional manifold.

Theorem 4.1.3 ([33], Theorems 5, 6): Consider the system $\dot{x} = f(t, x)$ with $f(t, 0) = 0$ written in the following cascaded form,

$$\dot{x}_1 = f_1(t, x_1) + g(t, x_1, x_2)x_2 \quad (4.9a)$$

$$\dot{x}_2 = f_2(t, x_2) \quad (4.9b)$$

where $x_1 \in \mathbb{R}^n$, $x_2 \in \mathbb{R}^m$, $f(t, x_1)$ is continuously differentiable function in (t, x_1) and $f_2(t, x_1)$, $g(t, x_1, x_2)$ are continuous in their arguments and locally Lipschitz in x_2 and (x_1, x_2) respectively. This system is a cascade of the following two subsystems,

$$\Sigma_1 : \dot{x}_1 = f_1(t, x_1) \quad \Sigma_2 : \dot{x}_2 = f_2(t, x_2) \quad (4.10)$$

in which the output of subsystem Σ_1 is perturbed by the output of subsystem Σ_2 .

Then,

- if the origin of the subsystems Σ_1 and Σ_2 are UGAS and solutions of the cascaded system in (4.9) remain bounded, the origin of the system (4.9) is UGAS. In addition, if the subsystems Σ_1 and Σ_2 are ULES, then the system in (4.9) is ULES.
- if the origin of subsystem Σ_1 is uniformly globally exponentially stable (UGES), the origin of the subsystem Σ_2 is ULES and UGAS, and

$$\|g(t, x)\| \leq k_1(\|x_2\|) + k_2(\|x_2\|)\|x_1\|,$$

then the origin of the cascaded system in (4.9) is ULES and UGAS.

4.2 Problem Formulation

The problem of re-designing the tracking controller as already stated in the Chapter 1 is defined again in this section. For re-designing the controller with the extended quadrotor model, it is assumed that a feasible reference trajectory given by $(\rho_r, R_r, \nu_r, \omega_r, f_r, \tau_r)$ satisfies the following dynamics,

$$\dot{\rho}_r = R_r \nu_r \quad (4.11a)$$

$$\dot{\nu}_r = -S(\omega_r)\nu_r - gR_r^T e_3 + \frac{f_r}{m}e_3 + \frac{\hat{F}_{r,aero}}{m} \quad (4.11b)$$

$$\dot{R}_r = R_r S(\omega_r) \quad (4.11c)$$

$$J\dot{\omega}_r = S(J\omega_r)\omega_r + \tau_r + \hat{M}_{r,d} + \hat{M}_{r,aero}, \quad (4.11d)$$

in which $0 < f_r^{\min} \leq f_r$.

The error coordinates of the extended quadrotor model defined on SE(3) are given by:

$$\begin{aligned} \tilde{\rho} &= R_r^T(\rho - \rho_r) & \tilde{R} &= R_r^T R \\ \tilde{\nu} &= -\tilde{R}^T S(\omega_r)\tilde{\rho} + \nu - \tilde{R}^T \nu_r & \tilde{\omega} &= \omega - \tilde{R}^T \omega_r, \end{aligned} \quad (4.12)$$

Problem 4.2.1 For $(\rho_r, R_r, \nu_r, \omega_r, f_r, \tau_r)$ being a given feasible reference trajectory, suitable control laws need to be determined for:

$$f = f(\rho, R, \nu, \omega, \rho_r, R_r, \nu_r, \omega_r) > 0 \quad (4.13a)$$

$$\tau = \tau(\rho, R, \nu, \omega, \rho_r, R_r, \nu_r, \omega_r), \quad (4.13b)$$

such that the resulting closed-loop system formed by (3.57)(4.11)(4.13), satisfies

$$\lim_{t \rightarrow \infty} \varepsilon(\tilde{\rho}(t), \tilde{R}(t), \tilde{\nu}(t), \tilde{\omega}(t)) = 0, \quad (4.14)$$

in which $\varepsilon(\tilde{\rho}, \tilde{R}, \tilde{\nu}, \tilde{\omega}) = \|\tilde{\rho}\| + \|\log \tilde{R}\| + \|\tilde{\nu}\| + \|\tilde{\omega}\|$, is the error measure.

4.3 Position Control Re-design

In this section, the position tracking controller for the quadrotor is derived. The quadrotor itself is an underactuated system and therefore we derive the position tracking controller by working under the assumption that the body-fixed linear accelerations can be used as virtual inputs. In the next section, the virtual inputs are realized to actual inputs in the design of the attitude tracking controller. The position tracking error is expressed in the body-fixed frame of reference which is given as [33],

$$\begin{aligned} \rho_e &= R_r^T(\rho_r - \rho) \\ \nu_e &= \nu_r - R_r^T R \dot{\nu} \end{aligned} \quad (4.15)$$

The position tracking error dynamics can then be given by,

$$\begin{aligned} \dot{\rho}_e &= -S(\omega_r)\rho_e + \nu_e \\ \dot{\nu}_e &= -S(\omega_r)\nu_e + \frac{f_r}{m}e_3 - R_r^T R \frac{f}{m}e_3 + \frac{1}{m}(\hat{F}_{r,aero} - R_r^T R \hat{F}_{aero}), \end{aligned} \quad (4.16)$$

where the term $\frac{f_r}{m}e_3 - R_r^T R \frac{f}{m}e_3$ is assumed to be the virtual input u for stabilizing the position tracking error dynamics. This is achieved by controlling the thrust magnitude and the attitude.

Assumption 4.3.1 For the control problem, we assume that the identified aerodynamic force model \hat{F}_{aero} to be bounded $\forall t$, which is given as,

$$\|\hat{F}_{aero,max}\| = D_{max}, \quad (4.17)$$

where D_{max} is a constant. This assumption is rather conservative and in the future a state dependent bound needs to be implemented for the disturbance forces.

Proposition 4.3.1 Consider the following dynamics,

$$\begin{aligned} \dot{\rho}_e &= -S(\omega_r)\rho_e + \nu_e \\ \dot{\nu}_e &= -S(\omega_r)\nu_e + \frac{1}{m}(\hat{F}_{r,aero} - R_r^T R \hat{F}_{aero}) + u \end{aligned} \quad (4.18)$$

in closed-loop with the dynamic state feedback consisting of the saturated PD controller term and the term for disturbance force compensation, given by,

$$u = -\sigma(k_\rho \rho_e + k_\nu \nu_e) - \frac{1}{m}(\hat{F}_{r,aero} - R_r^T R \hat{F}_{aero}) \quad (4.19)$$

where $k_\rho = k_\rho^T > 0$, $k_\nu = k_\nu^T > 0$. If $\omega_r(t)$ is bounded and continuous, then the origin of the closed loop system (4.18), (4.19) is UGAS.

Stability proof:

The closed loop system (4.18) and (4.19) can be described as follows:

$$\begin{aligned} \dot{\rho}_e &= -S(\omega_r)\rho_e + \nu_e \\ \dot{\nu}_e &= -S(\omega_r)\nu_e - \sigma(k_\rho \rho_e + k_\nu \nu_e) \end{aligned} \quad (4.20)$$

Consider the positive definite function defined by:

$$V_1(\rho_e, \nu_e) = V_\sigma(k_\rho \rho_e + k_\nu \nu_e) + \frac{k_\rho}{2} \nu_e^T \nu_e \quad (4.21)$$

where $V_\sigma(k_\rho \rho_e + k_\nu \nu_e)$ represents the integral of the proposed smooth saturated function which is positive definite and radially unbounded. The expression for (4.21) can then be written as,

$$V_1(\rho_e, \nu_e) = \int_0^{(k_\rho \rho_e + k_\nu \nu_e)} \sigma(s) ds + \frac{k_1}{2} \nu_e^T \nu_e \quad (4.22)$$

Along the solutions of (4.20), we get:

$$\begin{aligned} \dot{V}_1(\rho_e, \nu_e) &= \sigma(k_\rho \rho_e + k_\nu \nu_e)^T [-k_\rho S(\omega_r)\rho_e + k_\rho \nu_e - k_\nu S(\omega_r)\nu_e - k_\nu \sigma(k_\rho \rho_e + k_\nu \nu_e)] + \\ &\quad + k_\rho \nu_e^T [-S(\omega_r)\nu_e - \sigma(k_\rho \rho_e + k_\nu \nu_e)] \\ &= -k_\nu \sigma(k_\rho \rho_e + k_\nu \nu_e)^2 = Y_1(\rho_e, \nu_e) \leq 0 \end{aligned} \quad (4.23)$$

in which we have used the property $b^T S(\omega_r(t))b = 0$.

Also consider a continuous and bounded function, given by,

$$V_2(\rho_e, \nu_e) = \nu_e^T \rho_e \quad (4.24)$$

Then, $\dot{V}_2(\rho_e, \nu_e)$ is given by:

$$\dot{V}_2(\rho_e, \nu_e) = \nu_e^T \nu_e - \rho_e^T [\sigma(k_1 \rho_e + k_2 \nu_e)] = Y_2(\rho_e, \nu_e) \quad (4.25)$$

Applying Theorem 4.1.1, the system in (4.20) is UGAS.

4.4 Attitude Control Re-design

The virtual input u was assumed to be equal to $\frac{f_r}{m}e_3 - R_r^T R \frac{f}{m}e_3$ in the previous section. This resulted in stabilizing the position dynamics with u given in (4.19). In this section, the thrust f and torque τ inputs are used to let $R_r^T R f e_3$ converge to $f_r e_3 - mu$ with u as given in (4.19). To track a feasible reference trajectory we have the following condition,

$$0 < f_r^{\min} \leq f_r \quad (4.26)$$

To achieve this condition, it has to be guaranteed that $\|u\| < \frac{f_r^{\min}}{m}$. Since the reference aerodynamic force $\hat{F}_{r,aero}$ is bounded and considering Assumption 4.3.1 we have,

$$\|u\| \leq \alpha + d_{max} < \frac{f_r^{\min}}{m} \quad (4.27)$$

where d_{max} is a constant that bounds the term $\|\frac{1}{m}(\hat{F}_{r,aero} - R_r^T R \hat{F}_{aero})\| \forall t$ and α term depends on the choice of saturation function and gains k_ρ and k_ν . Since we have control over the value of α by choosing a proper saturation function and careful tuning of the gains, the condition in (4.27) can be satisfied and therefore a positive thrust given by $f > 0$ can be guaranteed.

The next step is to realize the control input for position subsystem into the attitude subsystem by defining thrust input f and a desired rotation matrix R_d which satisfies the following,

$$f R_d e_3 = f_r e_3 - mu \quad (4.28)$$

Since under a rotational transformation, the magnitude of a vector remains invariant, the thrust input f can be defined from (4.28) as follows,

$$f = \|f_r e_3 - mu\| \quad (4.29)$$

where u is given by (4.19) such that $f(t) > 0$. Now, the expression for torque input τ needs to be determined for achieving the desired attitude. The desired direction of the thrust vector is defined as,

$$R_d e_3 = \frac{f_r e_3 - mu}{\|f_r e_3 - mu\|} := f_d, \quad (4.30)$$

where, $f_d = [f_{d1} \ f_{d2} \ f_{d3}]^T$ which satisfies $f_{d3} > 0$. The rotation matrix R_d rotates the desired thrust vector f_d to the reference thrust vector (i.e., e_3) within the plane containing both vectors which can be given by,

$$R_d = \begin{bmatrix} 1 - \frac{f_{d1}^2}{1+f_{d3}} & -\frac{f_{d1}f_{d2}}{1+f_{d3}} & f_{d1} \\ -\frac{f_{d1}f_{d2}}{1+f_{d3}} & 1 - \frac{f_{d2}^2}{1+f_{d3}} & f_{d2} \\ -f_{d1} & f_{d2} & f_{d3} \end{bmatrix} \in \mathcal{SO}(3) \quad (4.31)$$

where it can be observed that a specific choice of yaw ψ is made. Similarly, the corresponding desired angular velocity ω_d can be given by,

$$\omega_d = \begin{bmatrix} -\dot{f}_{d2} + \frac{f_{d2}f_{d3}}{1+f_{d3}} \\ \dot{f}_{d1} - \frac{f_{d1}f_{d3}}{1+f_{d3}} \\ \frac{f_{d2}\dot{f}_{d1} + f_{d1}\dot{f}_{d2}}{1+f_{d3}} \end{bmatrix} \quad (4.32)$$

From (4.29) and (4.31), we obtain $f_r e_3 - mu = f R_d e_3$. Therefore, the initial aim to determine torque input τ such that $f R_r^T R$ converges to $f_r e_3 - mu$ is now substituted by the goal to determine τ such that $R^T R$ converge to R_d . Hence, the following error coordinates are considered for attitude tracking in the body-fixed frame of the quadrotor,

$$R_e = R_d^T (R_r^T R) \quad (4.33a)$$

$$\omega_e = \omega - R^T R_r \omega_r - R_e^T \omega_d \quad (4.33b)$$

The tracking error dynamics can then be defined by,

$$\begin{aligned} \dot{R}_e &= R_e S(\omega) \\ J\dot{\omega}_e &= S(J\omega)\omega + \tau + \hat{M}_d + \hat{M}_{aero} - JR^T R_r J^{-1} [S(J\omega)\omega + \tau_r + \hat{M}_{r,d} + \hat{M}_{r,aero}] \\ &\quad + J(S(\omega_e)[\omega - \omega_e] + JR_e^T [S(\omega_d)R_d^T \omega_r - \dot{\omega}_d]) \end{aligned} \quad (4.34)$$

The torque input τ is given by,

$$\begin{aligned} \tau &= -K_\omega \omega_e + K_R \sum_{i=1}^3 k_i (e_i \times R_e^T e_i) - J(S(\omega_e)[\omega - \omega_e] - JR_e^T [S(\omega_d)R_d^T \omega_r - \dot{\omega}_d]) \\ &\quad - S(J\omega)\omega - \hat{M}_d - \hat{M}_{aero} - JR^T R_r J^{-1} [S(J\omega)\omega + \tau_r + \hat{M}_{r,d} + \hat{M}_{r,aero}] \end{aligned} \quad (4.35)$$

which results in the following closed-loop form,

$$\dot{R}_e = R_e S(\omega) \quad (4.36a)$$

$$J\dot{\omega}_e = -K_\omega \omega_e + K_R \sum_{i=1}^3 k_i (e_i \times R_e^T e_i) \quad (4.36b)$$

for which according to Theorem 4.1.2, the origin $(I, 0)$ is ULES and UGAS for distinct $k_i > 0$ and $K_\omega = K_\omega^T > 0$ and $K_R = K_R^T > 0$.

4.5 Cascade Analysis

In this section, we perform the stability analysis of the closed-loop system. The controller outputs f and τ are determined in the previous section for asymptotic convergence of the desired control action for the position tracking error dynamics. The last step is to analyze the stability of the closed-loop cascaded system formed with the attitude controller and desired position controller.

The closed-loop dynamics with the extended model can written using the system dynamics in (3.57), the reference dynamics (4.11) in closed-loop with the stabilizing virtual input u (4.19), thrust f and (4.29) and torque τ (4.35). The resulting closed-loop system can be given by,

$$\dot{\rho}_e = -S(\omega_r)\rho_e + \nu_e \quad (4.37a)$$

$$\dot{\nu}_e = -S(\omega_r)\nu_e - \sigma(k_\rho \rho_e + k_\nu \nu_e) + \frac{f}{m} R_r^T R (R_e^T - I) e_3 \quad (4.37b)$$

$$\dot{R}_e = R_e S(\omega) \quad (4.37c)$$

$$J\dot{\omega}_e = -K_\omega \omega_e + K_R \sum_{i=1}^3 k_i (e_i \times R_e^T e_i) \quad (4.37d)$$

Proposition 4.5.1: If the gains k_ρ and k_ν are properly chosen such that $\|u\| \leq \frac{f_r^{\min}}{m}$, where $f_r^{\min} > 0$, then the origin $(\rho_e, \nu_e, R_e, \omega_e)$ of (4.37) is ULES and UaGAS.

Proof:

System (4.37) can be observed as a cascade of subsystem (4.37a), (4.37b) and subsystem (4.37c), (4.37d).

In Section 4.4, UaGAS of subsystem (4.37c), (4.37d) is proved and therefore we perform the stability analysis on $\mathbb{R}^6 \times \mathcal{G}$, where $\mathcal{G} \subset \mathcal{SO}(3) \times \mathbb{R}^3$ represents the almost global region of attraction of (4.37c), (4.37d).

The solutions of ρ_e and ν_e is initially proved to be bounded using the following Lyapunov candidate,

$$V = V_\sigma(k_\rho \rho_e + k_\nu \nu_e) + \frac{k_\rho}{2} \nu_e^T \nu_e \quad (4.38)$$

Differentiating (4.38) along the solutions of (4.37), gives,

$$\dot{V} \leq \nu_e^T \frac{f}{m} R_r^T R (R_e^T - I) e_3 \leq c_1 \sqrt{V_1} \|R_e - I\| \quad (4.39)$$

in which c_1 represents a constant. Since, the subsystem (4.37c), (4.37d) is ULES we have

$$\sqrt{V(t)} - \sqrt{V(t_0)} \leq c_2(t_0) \quad (4.40)$$

since V is found to be bounded along solutions, the solutions of (4.37) is therefore bounded as well based on the results of Theorem 4.1.3.

Corollary 4.5.1: The reference tracking problem is solved by the controller outputs consisting of virtual input u (4.19), thrust f (4.29) and torque τ (4.35).

Proof:

The position tracking errors $\rho_e \rightarrow 0$ and $\nu_e \rightarrow 0$ and therefore using (4.15) we have $\tilde{\rho} \rightarrow 0$ and $\tilde{\nu} \rightarrow 0$. Furthermore, since virtual input $u \rightarrow 0$, so from (4.30) we get the desired thrust $f_d \rightarrow 0$ and desired rotation matrix $R_d \rightarrow 0$.

We obtain $\tilde{R} \rightarrow 0$ from attitude tracking error R_e and (4.33a). At last, since $\dot{u} \rightarrow 0$, the desired angular velocity $\omega_d \rightarrow 0$. Therefore, angular velocity tracking error $\omega_e \rightarrow 0$ and using (4.33b) we get $\tilde{\omega} \rightarrow 0$.

4.6 Concluding Remarks

In this chapter, the previously designed tracking controller is updated for the extended quadrotor model. The natural cascaded structure in which the position subsystem is influenced attitude subsystem is utilized in designing of the position and the attitude controller. The position error dynamics defined in the tracking reference frame is stabilized using a virtual input. A saturated PD control action and a disturbance compensation term included in the virtual input ensures that the position subsystem is uniformly globally asymptotically stable in closed-loop. Lyapunov analysis along with the Nested Matrosov theorem is utilized in proving the stability of the position error dynamics. A non-negative bounded thrust is ensured by the assumption that the disturbance

forces are bounded and careful choice of saturation function. The derived control input for the position subsystem is realized into the attitude subsystem by defining a new set of attitude error coordinates. The attitude tracking error dynamics are stabilized in closed-loop by designing the torque input using Lyapunov theory. Resulting closed-loop torque input makes the attitude subsystem uniformly almost globally asymptotically stable. Lastly, the interconnected closed-loop system achieves uniform almost global asymptotic stability which is proved by cascade control theory.

Chapter 5

Simulation Study

The re-designed state-feedback controller is implemented in a simulation environment in this chapter. The tracking behaviour of the closed-loop system with a discretized controller needs to be analyzed through simulation. In Section 5.1, the tracking results of the identified extended model are compared with the actual quadrotor behaviour from the experimental results. The tracking performance of the updated controller from previous chapter is evaluated in Section 5.2 for the extended model in the simulation environment.

5.1 Validation of Extended Model

The extended model in the simulation environment is implemented with the parameters given in Table 5.1. The choice of the simulation step size is based on the Parrot AR Drone 2.0 on-board sensors outputting rate.

| Parameter | Description | Value | Unit |
|-----------|------------------------------------|----------------------|------------------|
| m | Quadrotor mass | 0.414 | kg |
| J_x | Moment of inertia around x -axis | 0.0022 | kgm ² |
| J_y | Moment of inertia around y -axis | 0.0025 | kgm ² |
| J_z | Moment of inertia around z -axis | 0.0045 | kgm ² |
| J_r | Rotor inertia | $2.12 \cdot 10^{-6}$ | kgm ² |
| T_s | Simulation step size | 0.0025 | s |

Table 5.1: Relevant simulation parameters.

During simulations, it was observed that the inclusion of the identified disturbance moment models \hat{M}_{aero} and \hat{M}_d had very little contribution to resemble the actual quadrotor behaviour and for fast time-varying trajectories, the simulation results diverged further away from the actual quadrotor behaviour. This can partially be attributed to the data utilized for the identification of roll and pitch moment models which are not informative enough to capture the true aerodynamic moments. To improve the moment models, further experiments need to be conducted with steady and high amplitudes of roll and pitch motions. For simulation purposes, the extended model in this chapter only accounts for the disturbance force model \hat{F}_{aero} and the disturbance moment models \hat{M}_{aero} and \hat{M}_d are made equal to zero.

The simulation with the extended model is performed with the previously designed non-linear controller in the work of [33]. The position tracking results are compared with the same controller gains used for the experiments which are presented in Table 5.2

| Parameter | Description | Value |
|------------|---------------|-------|
| k_w | Integral gain | 0.4 |
| k_z | Integral gain | 1 |
| k_ρ | Position gain | 3 |
| k_ν | Velocity gain | 2 |
| k_R | Attitude gain | 70 |
| k_ω | Attitude gain | 30 |
| k_1 | Attitude gain | 0.9 |
| k_2 | Attitude gain | 1 |
| k_3 | Attitude gain | 1.1 |

Table 5.2: Controller gains used for experiments and simulation

The quadrotor is made to follow a 3D circular reference trajectory with the extended model and the rigid body model in the simulation, which is given by,

$$\rho_r(t) = [\cos(a_t t) \quad \sin(a_t t) \quad 1.5 + \sin(a_t t)]^T \quad (5.1)$$

where the value of a_t is taken as 1 for a fast 3D circular maneuver. The initial conditions used for the simulation of the extended model and the rigid body model are given by,

$$\begin{aligned} \rho(t_0) &= \begin{bmatrix} 0.06 \\ 0.65 \\ 0.27 \end{bmatrix} & R(t_0) &= \begin{bmatrix} 1 & -0.0002 & -0.0003 \\ 0.0002 & 1 & -0.0070 \\ 0.0003 & 0.0070 & 1 \end{bmatrix} \\ \nu(t_0) &= \begin{bmatrix} 0.1 \\ -0.8 \\ 0.7 \end{bmatrix} & \omega(t_0) &= \begin{bmatrix} -0.5 \\ 0.3 \\ 0.1 \end{bmatrix} \end{aligned} \quad (5.2)$$

Figure 5.1 illustrates the position tracking performance of the quadrotor extended model rigid body model (red), rigid body model (blue) for the given 3D circular reference trajectory (dashed). Furthermore in Table 5.3, the RMS position error between the two models and the position measurement from the quadrotor experiments are given.

The actual quadrotor position measurements (black) can be compared with both the models from simulation in the figure. It is observed that the position measurements ρ of the rigid body model perfectly tracks given reference position ρ_r in the absence of external disturbances. However, the position measurement ρ of the extended model is more close to the actual quadrotor behaviour from experiments. In Table 5.3, it is observed that RMS position error is significantly less between the extended model and actual quadrotor than the RMS values for position error between the rigid body model and actual quadrotor. The extended model estimates the actual quadrotor x -position better than the rigid body model by almost 70%. In the y and z -direction, the results of the extended model are closer than the rigid body model to the actual quadrotor position by approximately 55%.

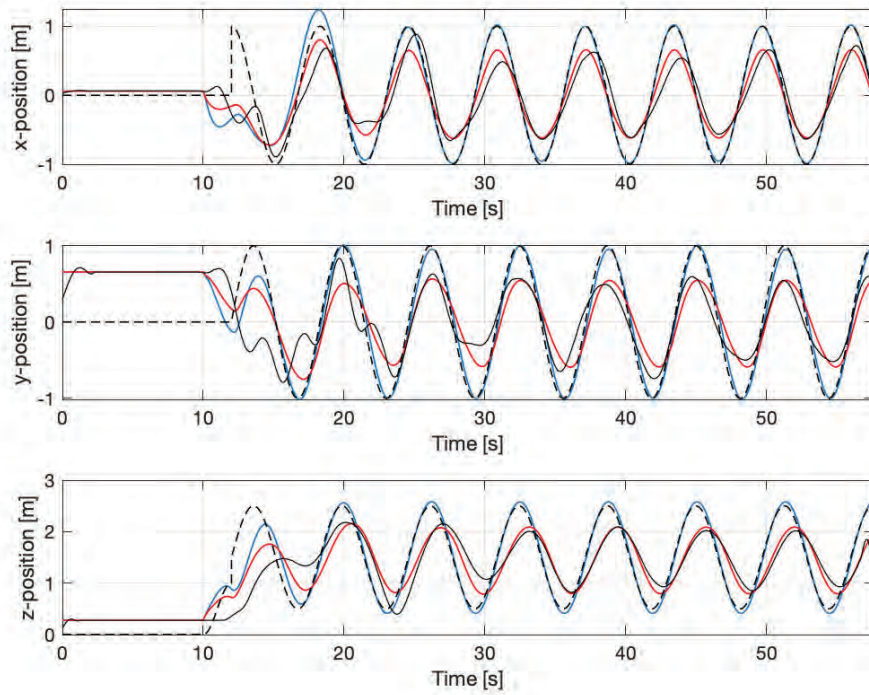


Figure 5.1: The simulation position measurements ρ for the extended model (red), rigid body model (blue) for the reference position ρ_r (dashed). In black, the filtered position measurements from quadrotor experiments for the same reference trajectory is provided for comparison.

| Model | RMS Position Error | | |
|------------------|--------------------|-------------------|-------------------|
| | x -position (m) | y -position (m) | z -position (m) |
| Rigid body model | 0.52 | 0.68 | 0.51 |
| Extended model | 0.15 | 0.28 | 0.22 |

Table 5.3: RMS position error between the models (rigid body model and extended model) and actual quadrotor measurement (shown in Figure 5.1).

The position measurements of the quadrotor is further evaluated for a reference trajectory with different speeds in x and z -directions using a vertical-eight-figure trajectory, given by,

$$\rho_r(t) = \begin{bmatrix} \sin(a_{t1}t) & 0 & 1 + 0.5 \sin(a_{t2}t) \end{bmatrix}^T, \quad (5.3)$$

where $a_{t1} = 1$ and $a_{t2} = 0.5$. The non-linear PID controller gains used for the simulation and the experiments are the same as given in Table 5.2. The initial conditions given in (5.8) are used again for the simulations models.

In Figure 5.2, the positions measurements ρ from simulation of the extended model (red) and rigid body model (blue) are compared to the experiment results (black) for the same reference position ρ_r (dashed) of vertical-eight-figure trajectory. In addition, the values of the RMS position error

in x and z direction between the actual quadrotor and the models are given in Table 5.4. The rigid body model efficiently tracks the reference position in absence of external disturbances. The extended model x -direction position measurement closely resembles the actual quadrotor position measurement from experiments. The z -direction measurement of the extended model from simulation is not however very close to the the experiment measurement, but the results appear to be better compared to the rigid body model position data. From the RMS values given in Table 5.4, the results of the extended model appear to be only closer to actual quadrotor position in x and z -direction by approximately 16% and 26%, respectively. The improvement in prediction by the extended model is observed to be less than the previously selected 3D circular trajectory. This is believed be caused by the reduced aerodynamic effects for the quadrotor following a slower time-varying trajectory.

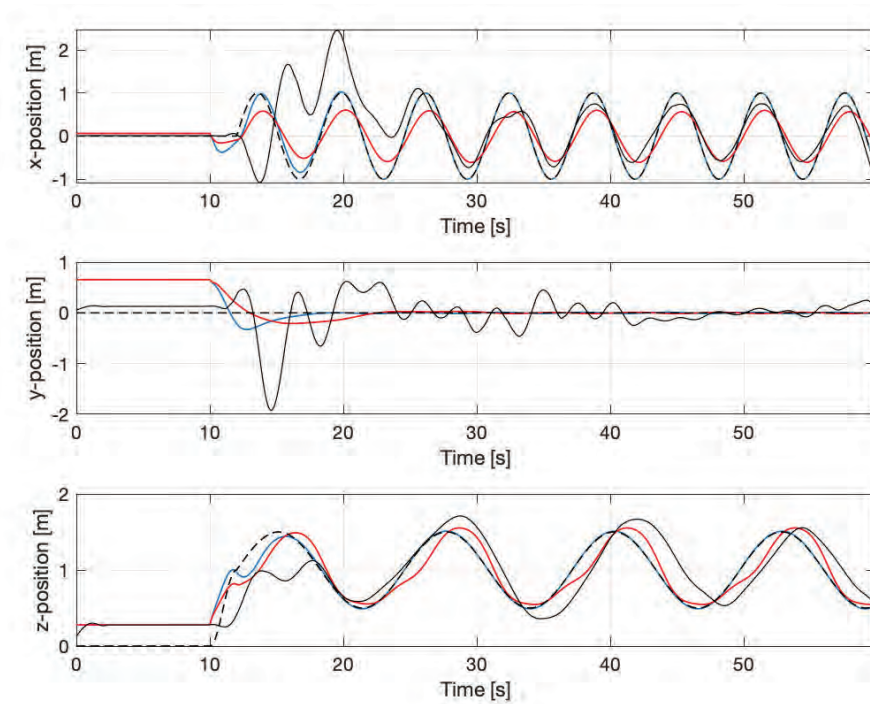


Figure 5.2: The simulation position measurements ρ for the extended model (red), rigid body model (blue) with vertical-eight-figure reference trajectory of position ρ_r (dashed). In black the actual quadrotor position measurements from experiments is given for the same reference trajectory.

| Model | RMS Position Error | |
|------------------|--------------------|-------------------|
| | x -position (m) | z -position (m) |
| Rigid body model | 0.4208 | 0.2720 |
| Extended model | 0.3506 | 0.1990 |

Table 5.4: RMS position error between the models (rigid body model and extended model) and actual quadrotor measurement (shown in Figure 5.2).

5.2 Re-designed Controller Simulation

The trajectory generation of the extended model is a challenging problem due to the inclusion of several complex terms. To determine a feasible reference trajectory from the given flat outputs of desired position (ρ_d) and heading (ψ_d), the extended dynamic model of the quadrotor should be differentially flat.

Considering the time limitations, the feasible reference trajectory in the simulation environment is generated by applying an open-loop input thrust f to the extended quadrotor model. For, $z_r = 1 + 0.5 \sin(t)$, the thrust input applied to the extended quadrotor model is given by,

$$f = m\sqrt{(\ddot{z}_r + g)^2}. \quad (5.4)$$

The initial conditions are set to the following values for generating the reference trajectory,

$$\begin{aligned} \rho(t_0) &= \begin{bmatrix} 5.6 \\ 3.9 \\ 4.6 \end{bmatrix} & R(t_0) &= \begin{bmatrix} 1 & -0.0011 & 0.0016 \\ 0.0011 & 1 & 0.0048 \\ -0.0016 & -0.0048 & 1 \end{bmatrix} \\ \nu(t_0) &= \begin{bmatrix} 0.1 \\ -0.8 \\ 0.7 \end{bmatrix} & \omega(t_0) &= \begin{bmatrix} 0 \\ 0 \\ 0 \end{bmatrix}. \end{aligned} \quad (5.5)$$

It is to be noted that the reference trajectory is generated without considering the disturbance moments. Consecutively, for the simulation of the updated controller in this chapter, the terms of disturbance moments \hat{M}_{aero} and \hat{M}_d and the corresponding reference terms $\hat{M}_{r,aero}$ and $\hat{M}_{r,d}$ are taken as zero. This implies that the stabilizing torque input τ derived in Chapter 4 is simplified to the following,

$$\begin{aligned} \tau = & -K_\omega \omega_e + K_R \sum_{i=1}^3 k_i (e_i \times R_e^T e_i) - J(S(\omega_e)[\omega - \omega_e] - J R_e^T [S(\omega_d) R_d^T \omega_r - \dot{\omega}_d] \\ & - S(J\omega)\omega - J R^T R_r J^{-1} [S(J\omega)\omega + \tau_r] \end{aligned} \quad (5.6)$$

The neglected disturbance moment terms however does not change the previously proved stability of the complete closed-loop cascaded system. Figure 5.3 shows the reference position ρ_r obtained from the simulation which satisfies the extended dynamic model of the quadrotor.

The quadrotor is made to track the obtained feasible reference trajectory using the saturated PD controller with disturbance compensation designed in Chapter 4. The saturation function in the controller is chosen as,

$$\sigma(k_\rho \rho_e + k_\nu \nu_e) = \frac{k_\rho \rho_e + k_\nu \nu_e}{\sqrt{1 + \|(k_\rho \rho_e + k_\nu \nu_e)\|^2}}, \quad (5.7)$$

where the position gain k_ρ and velocity gain k_ν used in the simulation are given in Table 5.5 along with the attitude controller gains.

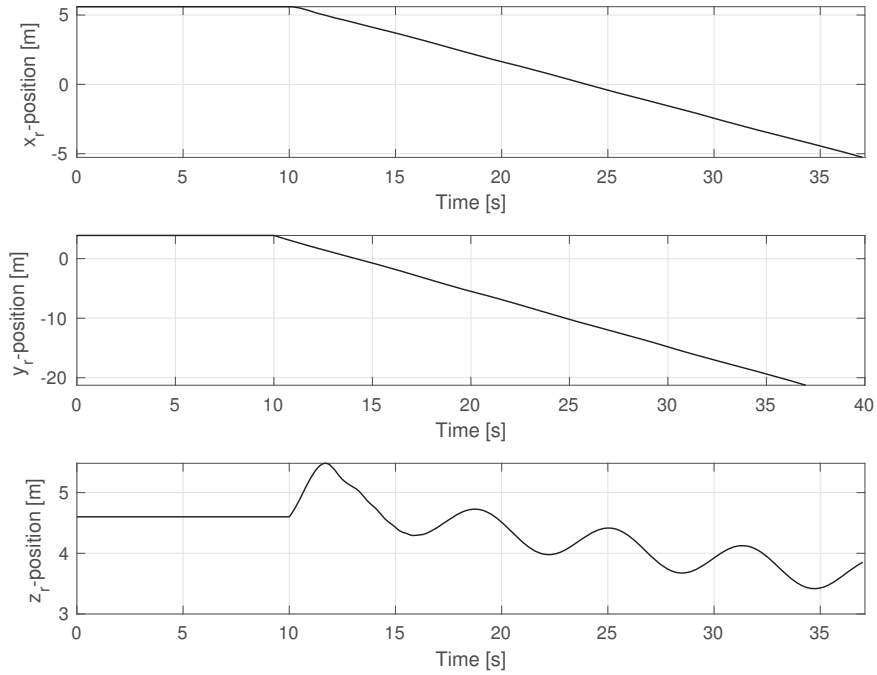


Figure 5.3: Reference position ρ_r satisfying the dynamics of the extended model.

| Parameter | Description | Value |
|------------|---------------|-------|
| k_ρ | Position gain | 3.8 |
| k_ν | Velocity gain | 6 |
| k_R | Attitude gain | 70 |
| k_ω | Attitude gain | 30 |
| k_1 | Attitude gain | 0.9 |
| k_2 | Attitude gain | 1 |
| k_3 | Attitude gain | 1.1 |

Table 5.5: Controller gains for the re-designed controller

The initial conditions for the simulation of the extended model with the re-designed controller is given by,

$$\begin{aligned}
 \rho(t_0) &= \begin{bmatrix} 4.4 \\ 3.3 \\ 3.6 \end{bmatrix} & R(t_0) &= \begin{bmatrix} 0.9983 & 0.0204 & -0.0544 \\ -0.0247 & 0.9965 & -0.0797 \\ 0.0525 & 0.0809 & 0.9953 \end{bmatrix} \\
 \nu(t_0) &= \begin{bmatrix} 0.1 \\ -0.8 \\ 0.7 \end{bmatrix} & \omega(t_0) &= \begin{bmatrix} 0 \\ 0 \\ 0 \end{bmatrix}
 \end{aligned} \tag{5.8}$$

In Figure 5.4, the position measurement of the extended model using the re-designed controller is presented. The position measurement in blue represents the quadrotor trajectory with no distur-

balance force compensation term included in the controller. This implies that the term $\frac{1}{m}(\hat{F}_{r,aero} - R_r^T R \hat{F}_{aero})$ is set to zero in the virtual input u . The position data in red represents the tracking performance with the disturbance compensation term included. It is clearly seen that addition of the disturbance compensation term resulted in improved tracking of the reference position ρ_r (in black).

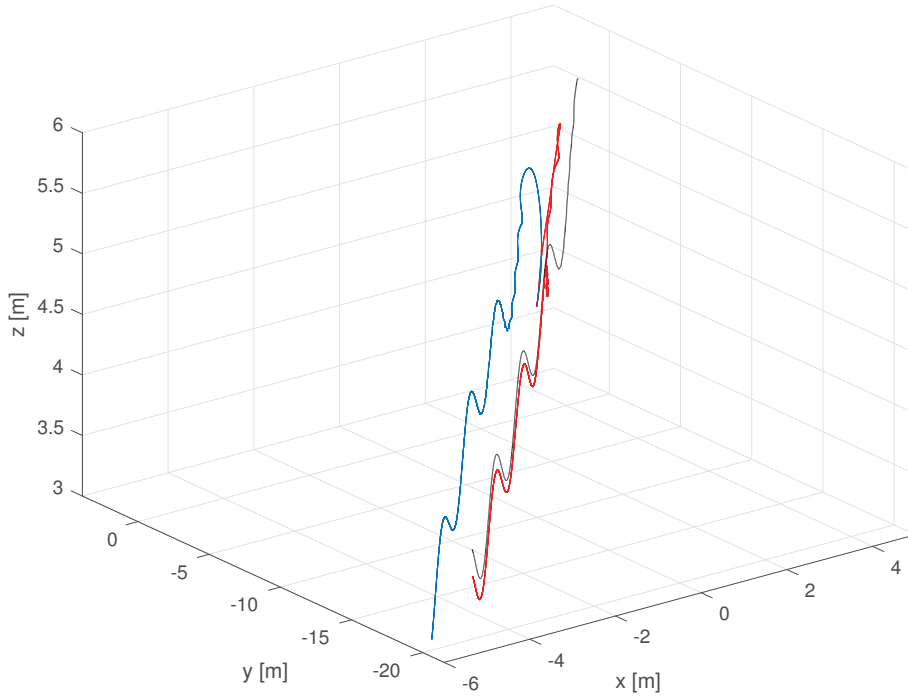


Figure 5.4: 3D representation for the quadrotor flight trajectory for position reference ρ_r (black). The trajectory in blue represents the tracking performance with no disturbance compensation and the red trajectory represents the tracking performance with disturbance compensation.

The position error of the controller with and without compensation for external disturbance is shown in Figure 5.5. In the figure it is observed that with zero disturbance compensation there exists a constant error (in blue) from the given reference trajectory. The position error (in red) converges close to zero with the re-designed controller including external aerodynamic force compensation.

It can be recalled that the attitude error in the previous chapter is defined by $R_e = R_d^T (R_r^T R)$, which asymptotically converges to I . Here, the distance of R_e to I is represented by the following natural Riemannian metric, given by,

$$d(R_r^T R, R_d) = \|\log(R_e)\| \quad (5.9)$$

This metric restricts the values in the range of $[0, \pi)$. The attitude error with and without external disturbance compensation is given in Figure 5.6 which is given by $|\log(R_e)|$. It can be seen that for desired reference R_d with and without the disturbance compensation, the attitude error (in red) converges to zero which represents the convergence of the term $R_r^T R$ to R_d .

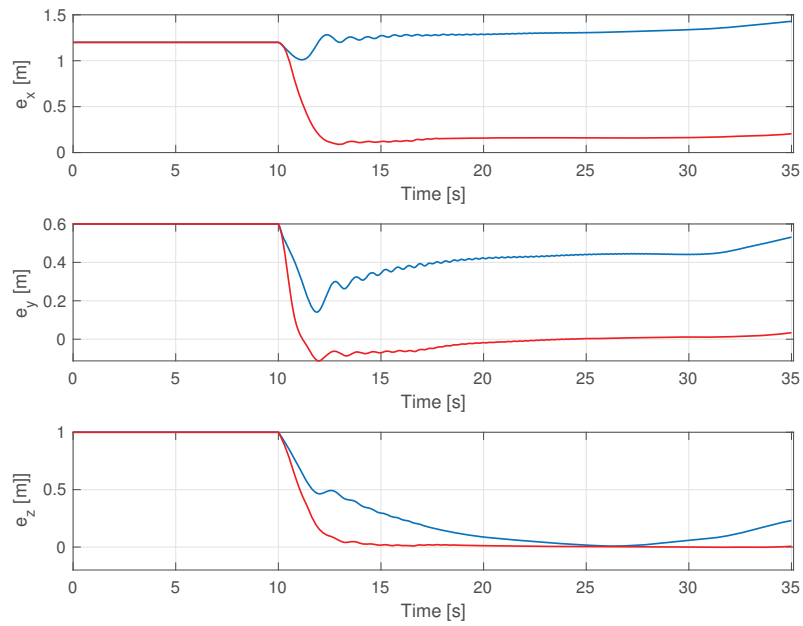


Figure 5.5: Position error $e_\rho = \rho_r - \rho$ with external disturbance force compensation (red) and without compensation for disturbance (blue).

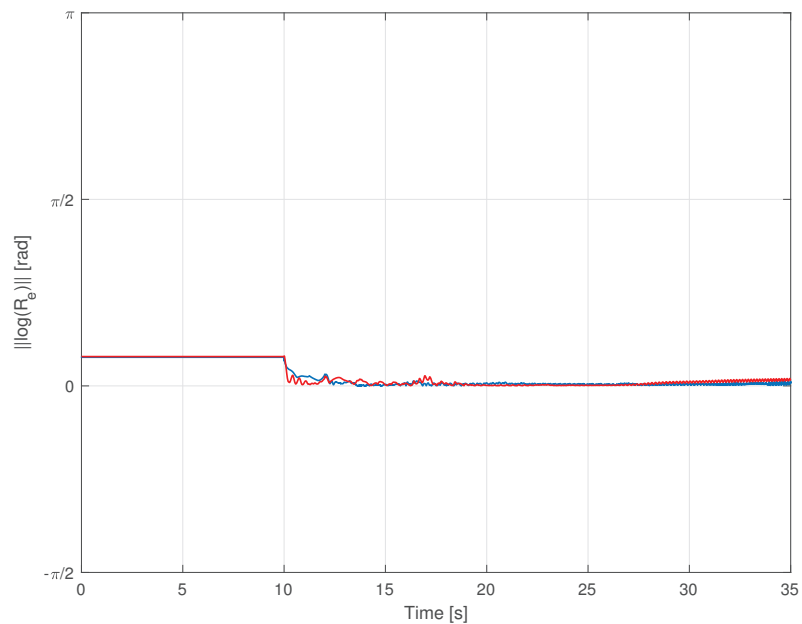


Figure 5.6: Attitude error representing $R_r^T R$ converging to R_d using the natural Riemannian metric. The attitude error with and without external disturbance compensation are given in red and blue, respectively.

5.3 Concluding Remarks

This chapter studies the performance of the re-designed controller for the extended model in a simulation environment. Initially, the behaviour of the extended model in simulation is compared to the experimental results of the quadrotor. The reference trajectories used for simulation and experiment include a fast time varying 3D circular trajectory and a vertical-eight-figure trajectory. It was observed that the position measurements of the extended model closely resemble the actual position of quadrotor using the previously designed controller. The identified moment model seemed to perform poorly and was therefore neglected from the simulation model and also the updated controller. The tracking performance of the re-designed controller is determined for the extended model with particular choice of control gains and initial conditions. The complexity of the extended model makes trajectory generation more complicated and therefore for present simulation needs, the trajectory is generated in the simulation environment with an open loop input thrust. It was observed that the disturbance compensation term in the controller enables the quadrotor in simulation to track the feasible reference trajectory with sufficient accuracy. With the exclusion of the disturbance force compensation term, the quadrotor maintained some offset from the given reference.

Chapter 6

Conclusions and Recommendations

The thesis report has addressed the problem of tracking control of quadrotor subjected to external disturbances. Models capable of capturing most of the actual dynamic behaviour of the quadrotor system are significant for the design of autonomous tracking controllers. An extended model is determined in this project using techniques from data-driven modeling. The resulting extended model is incorporated into the previous design of a nonlinear controller for improving the tracking of fast time-varying trajectories.

6.1 Conclusions

The results from the thesis report are discussed based on the research conducted for model identification and control design. The simulations conducted based on the final results are also briefly mentioned.

Model Identification and Control

The identification procedure starts from gathering the relevant data from the available data acquisition system. For identifying the disturbance model, information on quadrotor rotor speed and body-fixed linear velocities are not directly obtained. The rotation speed of the rotors is determined from the inputs applied to the quadrotor. Quadrotor body-fixed velocity is obtained using the external camera outputs and an almost globally stable attitude observer. Derivatives of position estimates from the camera and the reconstructed attitude are used to get the quadrotor velocity estimate in body-fixed frame.

The second step of identification involves defining grey-box model structures for the disturbance forces and moments acting externally on the quadrotor. A lumped parameter model is formed based on the existing theoretical models on aerodynamics. In data-driven modeling, it is crucial to consider only the most relevant model terms using methods like model selection. A modified version of the Least Angle Regression Algorithm is used to select the suitable set of model predictor terms for the disturbance model. Outputs of the Inertial Measurement Unit from tailored experiments are used to retrieve the measurements on disturbance forces and moments.

The identified disturbance model is incorporated into the previous design of the cascaded controller with a few modifications. The position and velocity tracking errors are defined in a fixed reference frame of the quadrotor for the trajectory control problem. For position control, the stabilizing

virtual input consists of a saturated PD control action and another term for compensation of the external disturbance forces. A non-negative thrust is then ensured by assuming the disturbance force to be bounded and by taking a suitable saturation function. The bounded input for position control is realized into the attitude controller by defining a rotation matrix in the desired reference frame. The attitude error dynamics are correspondingly defined for stabilizing the position and attitude subsystem in closed-loop by determining a proper torque input. Lyapunov stability theory is used to determine the inputs which make the closed-loop position subsystem and attitude subsystem *uniformly globally asymptotically stable* and *uniformly almost globally asymptotically stable*, respectively. The stability of the complete cascaded closed-loop system is finally proved using cascade control theory.

Simulation

A comparison of the position measurements from the extended model in simulation was made with the previously conducted quadrotor experiments. The identified disturbance moment model was neglected from the simulation model and the controller, as it generated undesired results caused by poor identification data. For different fast time-varying trajectories it was observed that the position results of the extended model closely resembled the results of the actual quadrotor system. The re-designed controller is implemented in the simulation environment for a feasible reference trajectory generated by applying an open loop thrust. Position measurements of the simulation model in closed-loop show that the drone is capable of tracking the given trajectory with sufficient accuracy. The previously incorporated integral action is no longer required in the controller since it already takes into consideration most of the external disturbances acting on the drone.

6.2 Recommendations

This section covers the recommendations for future work and practical implementation in the following points,

- The proposed attitude observer can be used for real time applications by implementing the quaternion version of the kinematic observer using first order Euler integration. By carefully choosing the gains and the initial conditions, stable unbiased attitude responses can be obtained.
- For the identification the quadrotor rotor speed was obtained using PWM motor inputs. A much more accurate method would be to determine the rotor speed by identification of a motor model. A first order system with non-linear parameters can be determined with input as applied voltage and the rotor rotation speed as output. The model parameter estimates can then be obtained using optimization methods such as nonlinear least squares. Experiments can be performed to manually measure the rotor rotation speed while the quadrotor is fixed to the ground and the applied voltage data is available from the on-board sensors.
- The identified moment models performed poorly due to lack of good experimental data for parameter estimation. For proper identification of moment models, experiments need to be conducted such that the quadrotor performs steady and high magnitude angular maneuvers.

- In the re-design of the controller, the disturbance forces were assumed to be bounded by a constant to ensure a non-negative and bounded control thrust. This assumption is rather conservative and in the future a state dependent bound needs to be established for the stability derivation of the controller. For example, the dissipativity property of drag forces suggest that the intensity of the quadrotor drag forces cannot be larger than the velocity vector of the vehicle.
- The trajectory generation of the extended model is a difficult problem due to the presence of several complex terms in the quadrotor dynamics. Methods from differential flatness theory such as feedback linearization could be implemented to determine the reference states and inputs from desired position and heading angle.
- The practical implementation of the re-designed controller is hindered by the time limitations of the project and also the lack of a velocity observer. The problem of determining the quadrotor body-velocity can be addressed by either updating the previously proposed velocity error observer with the identified disturbance forces or building a new velocity observer which takes into consideration all the external forces acting on the drone.

Bibliography

- [1] A. K. Saha, J. Saha, R. Ray, S. Sircar, S. Dutta, S. P. Chattopadhyay and H. N. Saha “IOT-based drone for improvement of crop quality in agricultural field,” *IEEE 8th Annual Computing and Communication Workshop and Conference (CCWC)*, 612-615, January 2018.
- [2] Chong Huang, Fei Gao, Jie Pan, Zhenyu Yang, Weihao Qi, Peng Chen, Xin Yang, Shaojie Shen and Kwang-Ting Cheng, “ACT: An Autonomous Drone Cinematography System for Action Scenes,” *IEEE International Conference on Robotics and Automation (ICRA)*, 7039-7046, May 2018.
- [3] S. Zacharek, “How Drones Are Revolutionizing the Way Film and Television Is Made,” article, *TIME, Entertainment*, May 2018.
- [4] Constantine Samaras and Joshua Stolaroff, “Delivering packages with drones might be good for the environment,” *The Conversation*, February 2018.
- [5] Anne Goodchild and Jordan Toy, “Delivery by drone: An evaluation of unmanned aerial vehicle technology in reducing CO2 emissions in the delivery service industry,” *Transportation Research Part D*, 58-67, June 2018.
- [6] Sudipta Chowdhury, Adindu Emelogu, Mohammad Marufuzzaman, Sarah G. Nurre and Linkan Bian, “Drones for disaster response and relief operations: A continuous approximation model,” *International Journal of Production Economics*, 167-184, 2017.
- [7] Martin Rosalie, Grégoire Danoy, Pascal Bouvry and Serge Chaumette, “UAV Multilevel Swarms for Situation Management,” *Proceedings of the 2nd Workshop on Micro Aerial Vehicle Networks, Systems, and Applications for Civilian Use*, 49-52, 2016.
- [8] Jack Williams, “Into the Eye: Tracing the History of the Hurricane Hunters,” *Weatherwise*, 37-45, 2015.
- [9] R. Mahony, V. Kumar, and P. Corke, “Multirotor aerial vehicles: modeling, estimation, and control of quadrotor,” *IEEE Robotics and Automation Magazine*, vol. 19, no. 3, pp. 20–32, 2012.
- [10] H. Huang, G. M. Hoffmann, S. L. Waslander, and C. J. Tomlin, “Aerodynamics and control of autonomous quadrotor helicopters in aggressive maneuvering”, *IEEE Conference on Robotics and Automations*, pp. 3277-3282, 2009.
- [11] Sammy Omari, Minh-Duc Hua, Guillaume Ducard, “Nonlinear Control of VTOL UAVs Incorporating Flapping Dynamics”, *IEEE/RSJ International Conference on Intelligent Robots and Systems*, November 2013.

- [12] H.J.K. de Kleuver, "Extended non linear dynamics for quadrotor control in aggressive maneuvering," master's thesis [DC report, 2017.092], Eindhoven University of Technology, Dynamics and Control Group, Department of Mechanical Engineering, Eindhoven, the Netherlands, October 2017.
- [13] Xiaodong Zhang, Xiaoli Li, Kang Wang and Yanjun Lu, "A Survey of Modelling and Identification of Quadrotor Robot", *Abstract and Applied Analysis*, October 2014.
- [14] M.-D. Hua, T. Hamel, and C. Samson, "Introduction to feedback control of underactuated VTOL vehicles," *IEEE Control Systems Magazine*, pp. 61–75, 2013.
- [15] M. Bergamasco and M. Lovera, "Identification of Linear Models for the Dynamics of a Hovering Quadrotor", *IEEE Trans Control Systems Technology*, vol. 22, pp. 1696-1707, 2014.
- [16] Pietro Panizza, Fabio Riccardi, Marco Lovera, "Black-box and grey-box identification of the attitude dynamics for a variable-pitch quadrotor", *Conference: Workshop on Advanced Control and Navigation for Autonomous Aerospace Vehicles*, June 2015.
- [17] J. Muliadi and B. Kusumopu, "Assessing The Method of State Space Determination from the Quadrotor Flight Simulation", *International Seminar on Application for Technology of Information and Communication (iSemantic)*, pp. 258-263, 2017.
- [18] Lennart Ljung, "Prediction Error Estimation Methods", Technical Report, Department of Electrical Engineering, Linköping University, 2001.
- [19] Ingrid Kugelberg, "Black-Box Modeling and Attitude Control of a Quadcopter", Master Thesis, Department of Electrical Engineering, Linköping University, 2016.
- [20] Ionel Stanculeanu, Theodor Borangiu, "Quadrotor Black-Box System Identification", *World Academy of Science, Engineering and Technology*, 2011.
- [21] Pairan, M.F. and Shamsudin, S.S., "System identification of an unmanned quadcopter system using MRAN neural", *IOP Conference Series: Materials Science and Engineering*, 2017.
- [22] Derek Scott Miller, "Open Loop System Identification of a Micro Quadrotor Helicopter from Closed Loop Data", Master Thesis, University of Maryland, College Park, 2011.
- [23] G. Gremillion, "System identification of a quadrotor micro air vehicle," *Proceedings of the AIAA Atmospheric Flight Mechanics Conference*, p. 7644, Toronto, Canada, 2010.
- [24] G. Cai, H. Mehairi, H. Al-Hosani, J. Dias and L. Seneviratne, "Frequency-Domain Flight Dynamics Model Identification of MAVs - Miniature Quad-Rotor Aerial Vehicles", *IEEE/RSJ International Conference on Intelligent Robots and Systems*, pp. 3376-3381, 2014.
- [25] O. Prot, and J. Ramos, "Identification of parameterized gray-box state-space systems: From a black-box linear time-invariant representation to a structured one" in *IEEE Transactions On Automatic Control*, vol. 59, no. 11, November 2014.
- [26] J. Yang, Z. Cai, Q. Lin, D. Zhang and Y. Wang, "System Identification of Quadrotor UAV Based on Genetic Algorithm", *IEEE Chinese Guidance, Navigation and Control Conference (CGNCC)*, pp. 2336-2340, 2014.

- [27] M. Alkowitz, V. Becerra and W. Holderbaum, “Body-centric Modelling, Identification, and Acceleration Tracking Control of a Quadrotor UAV”, *International Journal of Modelling Identification and Control*, vol. 24, pp. 29-41, 2015.
- [28] Rajan Gill and Raffaello D’Andrea, “Propeller Thrust and Drag in Forward Flight”, *IEEE Conference on Control Technology and Applications*, August 2017.
- [29] James Svacha, Kartik Mohta, Vijay Kumar, “Improving Quadrotor Trajectory Tracking by Compensating for Aerodynamic Effects”, *International Conference on Unmanned Aircraft Systems (ICUAS)*, June 2017.
- [30] D. Derya Kaya, “Modeling and Experimental Identification of Quadrotor Aerodynamics”, Master Thesis, *Aerospace Engineering Department, Middle East Technical University*, August 2014.
- [31] Sihao Sun, Coen De Visser and Rudi Schilder, “Identification of Quadrotor Aerodynamic Model from High Speed Flight Data”, *AIAA Atmospheric Flight Mechanics Conference*, January 2018.
- [32] S. J. A. M. van der Eijnden, “Cascade based tracking control of quadrotors,” master’s thesis [DC report, 2017.012], Eindhoven University of Technology, Dynamics and Control Group, Department of Mechanical Engineering, Eindhoven, the Netherlands, January 2017.
- [33] E. Lefeber, S. J. A. M. van der Eijnden, and H. Nijmeijer, “Almost global tracking control of a quadrotor uav on $se(3)$,” in *56th IEEE Conference on Decision and Control, Melbourne, Australia*, 2017.
- [34] Mahony, R., Hamel, T., & Pfimlin, J. M., “Nonlinear complementary filters on the special orthogonal group.”, *IEEE Transactions on automatic control*, 53(5), 1203-1218., (2008).
- [35] N. Jeurgens, “Identification and control implementation of an AR Drone 2.0”, Master’s thesis, Eindhoven University of Technology, 2017, Department of Mechanical Engineering, DC 2017.013.
- [36] Sihao Sun, Coen C. de Visser and Qiping Chu, “Quadrotor Gray-Box Model Identification from High-Speed Flight Data” *JOURNAL OF AIRCRAFT* , November 24, 2018.
- [37] Manon Kok, Jeroen D. Hol and Thomas B.Schon , “Inertial Sensors for Position and Orientation Estimation,” *Foundations and Trends in Signal*, Vol. 11: No. 1-2, pp 1-153, 2017
- [38] Burak Yüksel, Cristian Secchi, Heinrich H Bülthoff, Antonio Franchi, “ A nonlinear force observer for quadrotors and application to physical interactive tasks”, *IEEE/ASME International Conference on Advanced Intelligent Mechatronics*, Jul 2014, Besancon, France. 8p., 2014.
- [39] Bradley Efron, Trevor Hastie, Iain Johnstone and Robert Tibshirani, “Least angle regression”, *Annals of Statistics*, 32(2), 407–499, 2004.
- [40] T. Lombaerts, “Model-based fault detection and identification with online aerodynamic model structure selection”, *Progress in Flight Dynamics, GNC, and Avionics*, 299-316, 2013.
- [41] Trevor Hastie, Jonathan Taylor, Robert Tibshirani and Guenther Walthe, “Forward stagewise regression and the monotone lasso”, *Electronic Journal of Statistics*, 1–29, 2007.
- [42] Caitlin Powers, Daniel Mellinger, Aleksandr Kushleyev, Bruce Kothmann, and Vijay Kumar, “Influence of aerodynamics and proximity effects in quadrotor flight.”, *In Experimental robotics*, pages 289-302. Springer, 2013.

- [43] Mor Gilad, Inderjit Chopra and Omri Rand, “Performance Evaluation of a Flexible Rotor in Extreme Ground Effect.”, *37th European Rotorcraft Forum, Milan, Italy*, 2011.
- [44] M Bangura R Mahony, “Nonlinear Dynamic Modeling for High Performance Control of a Quadrotor”, *Australasian Conference on Robotics and Automation*, Australian Robotics and Automation Association, Wellington, pp. 1-10, 2012.
- [45] Sanne Marx, “High Performance Drone Target Pursuit”, Master’s thesis, Eindhoven University of Technology, 2017, Department of Mechanical Engineering, CST 2017.017.
- [46] H. K. Khalil, *Nonlinear Systems*. Prentice Hall, 3 ed., December 2001.
- [47] A. Loría, E. Panteley, and A. Teel, “A nested Matrosov theorem and persistency of excitation for uniform convergence in stable nonautonomous systems,” *IEEE Transactions on Automatic Control*, vol. 50, no. 2, pp. 183–198, 2005.
- [48] Michael Lynch, Kevin Robinson, Ovidiu Ghita, Paul F. Whelan, “A Performance Characterisation In Advanced Smoothing Techniques”, *Vision Systems Group*, Dublin City University, Ireland.
- [49] Srinivasan Rajagopalan, Richard Robb, “Image smoothing with Savitzky-Golay filters”, *Proceedings of SPIE - The International Society for Optical Engineering*, San Diego, CA, 2003.
- [50] Thomas F. Edgar, “Recursive Least Squares Parameter Estimation for Linear Steady State and Dynamic Models,” Department of Chemical Engineering University of Texas, Austin.

Appendix A

Attitude Observer Simulation

The performance of the proposed explicit complementary filter with bias correction is evaluated in this appendix for the data obtained from quadrotor experiments. Following initial conditions are chosen for the almost globally stable attitude observer,

$$\hat{R}(t_0) = I \quad \hat{b}(t_0) = [0, 0, 0]^T \quad \hat{v}_a(t_0) = [0.09, 0.005, 0.996]^T \quad (\text{A.1})$$

The gains are selected as, $k_P = 1 \text{ rad.s}^{-1}$ and $k_I = 0.3 \cdot 10^{-4} \text{ rad.s}^{-1}$. Figure A.1 shows the roll, pitch and yaw angles from open loop integration of gyro outputs (dashed in blue) and the reconstructed \hat{R} of the observer (red).

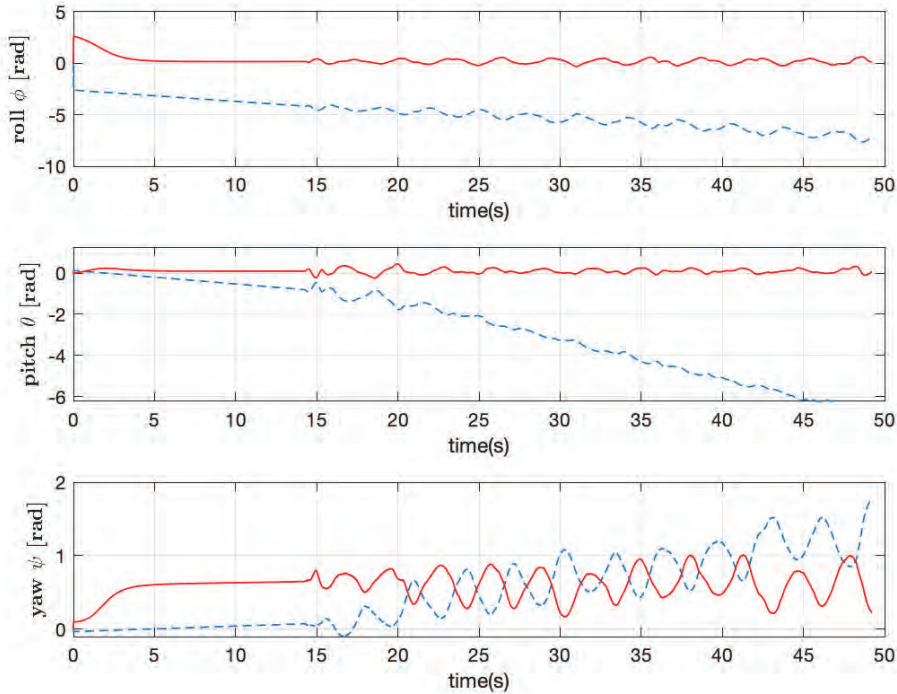


Figure A.1: Attitude estimates from open loop integration of gyro outputs (dashed in blue) and explicit complementary filter with bias correction (in red) .

In Figure A.1, it can be observed that the open-loop integrated attitude has the presence of a time varying bias. The explicit complementary filter has generated unbiased estimates of the quadrotor attitude for specific choice of gains.

The error measure E_{mes} of the filter is expressed as:

$$E_{mes} = 1 - \langle v_a, \hat{v}_a \rangle = 1 - \text{tr}(v_a^T \hat{v}_a) \quad (\text{A.2})$$

Figure A.2 shows the error measure obtained for the observer implemented on the flight data from experiments.

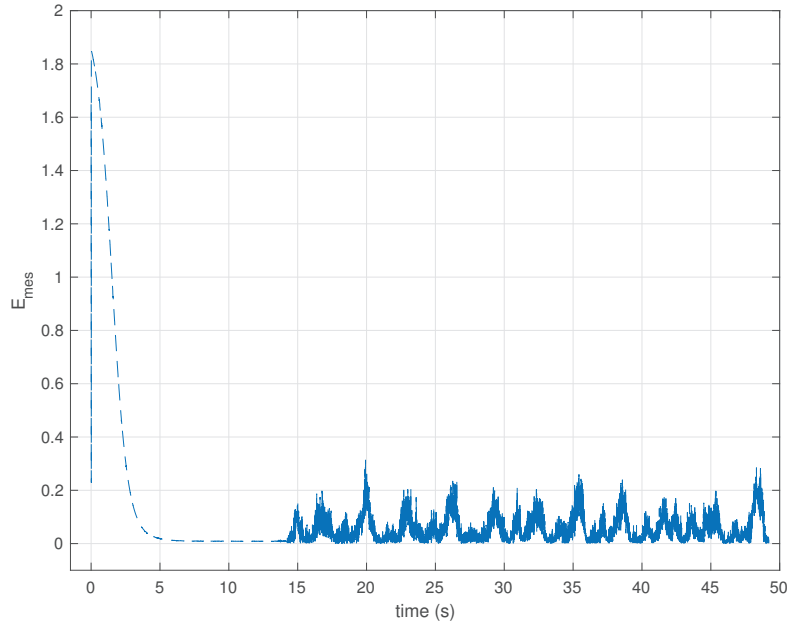


Figure A.2: Error measure E_{mes} for explicit complementary filter with bias correction.

It is observed in Figure A.2 has a constant offset of around 0.2 from zero, this is caused by the presence of noise in the normalized accelerometer measurements.

Appendix B

Differentiation Filter

The working of the Savitzky Golay filter is briefly explained here which is used for smoothing position data and for computing the numerical derivatives as mentioned in 2.2. The filter basically replaces each value of the data point with the value of a chosen fitted polynomial (using least-squares). The procedure involves finding the coefficients of the chosen polynomial which are linear to the data values. This is implemented by computing coefficients of fictitious data and applying filter over all the data points.

Assuming the size of the smoothing window is $N \times N$ where N is odd, and order of polynomial used for fitting is k , where $N > k + 1$. The smoothing causal filter is usually expressed as [48],

$$g_{x,y} = \sum_{j=-n}^n \sum_{i=-n}^n C_{i,j} f_{x+i,y+i} \quad (\text{B.1})$$

where C is the convolution matrix and f_{xy} is the real data and $n = \frac{N-1}{2}$. Suppose we have to fit a polynomial of the following type to the data,

$$f(x_i, y_i) = a_{00} + a_{10}x_i + a_{01}y_i + a_{20}x_i^2 + a_{11}x_iy_i + a_{02}y_i^2 + \dots + a_{0k}y_i^k \quad (\text{B.2})$$

Using least-squares the vector of coefficients $a = [a_{00}, a_{01}, a_{10} \dots a_{0k}]^T$ can be computed. For the general equation given by,

$$A \cdot a = f \quad (\text{B.3})$$

the vector a is computed by,

$$a = (A^T \cdot A)^{-1} \cdot (A^T f) \quad (\text{B.4})$$

Since least-squares fitting is linear to the values of the data, the coefficients can be computed despite of the actual data. This is achieved by replacing f in (B.4) by a unit vector. Thus the coefficient matrix C becomes, $C = (A^T A)^{-1} (A^T)$. C can be set back to the traditional looking filter of size $N \times N$. The first coefficient is used to smooth the data and the higher order coefficients are implemented to compute numerical derivatives. It is to be noted that the above expressions are used for filtering of images consisting of both x and y data points together.

Appendix C

Hovering Thrust model

The estimate of the hovering parameter κ is estimated in Section 3.2 using eight different hovering flight experiments. Here in this appendix, the estimate of κ is presented for each of the eight flight experiments (with different dataset length) in Table C.1.

| Flight Experiment No. | Length of Dataset | Value of κ |
|-----------------------|-------------------|------------------------|
| 1 | 19160 | $6.861 \cdot 10^{-06}$ |
| 2 | 10070 | $6.824 \cdot 10^{-06}$ |
| 3 | 18812 | $6.732 \cdot 10^{-06}$ |
| 4 | 4550 | $6.984 \cdot 10^{-06}$ |
| 5 | 15993 | $6.993 \cdot 10^{-06}$ |
| 6 | 14096 | $6.854 \cdot 10^{-06}$ |
| 7 | 19352 | $6.880 \cdot 10^{-06}$ |
| 8 | 19291 | $6.833 \cdot 10^{-06}$ |

Table C.1: Estimate of κ from each hovering experiment

It is seen in Table C.1 that the κ estimate differs for each hovering experiment. This is very much expected since during experiments the drone did not hover completely motionless at a stationary point.

In some of the experiments the drone was slowly moving in the x - y plane and in other experiments the drone was slowly moving up and down in the vertical direction. These variations does influence the estimate of parameter κ which can seen from the expressing for thrust model given in Section 3.2.

Appendix D

RLS Algorithm

The hovering thrust parameter κ from Section 3.2 is estimated from the Recursive least square algorithm explain in this Appendix.

For model $y = ax$ with the response variable data $y^* = ax + \epsilon$, the least square estimate of a for i^{th} data point (y_i, x_i) is given by:

$$\min_{\hat{a}} \sum_{i=1}^k (y_i^* - \hat{a}x_i)^2 \quad (\text{D.1})$$

The solution for the minimum (least squares) estimate is given by (non-sequential):

$$\hat{a}_k = \underbrace{\left(\sum_{i=1}^k x_i^2\right)^{-1}}_{p_k} \underbrace{\left(\sum_{i=1}^k x_i y_i\right)}_{b_k} \quad (\text{D.2})$$

where p_k and b_k are functions of number of samples.

The sequential form of (D.2) for new data point x_i and y_i is given by:

$$\begin{aligned} p_k^{-1} &= \sum_{i=1}^k x_i^2 = p_{k-1}^{-1} + x_k^2 \\ b_k &= \sum_{i=1}^k x_i y_i = b_{k-1} + x_k y_k \end{aligned} \quad (\text{D.3})$$

The recursive form for parameter estimation is hence given by [50]:

$$\hat{a}_k = \hat{a}_{k-1} - K_k \underbrace{(x_k \hat{a}_{k-1} - y_k)}_{\text{estimation error}} \quad (\text{D.4})$$

$$\text{where, } K_k = \frac{p_{k-1} x_k}{(1 + p_{k-1} x_k^2)}$$

The update for p_k is given by:

$$p_k = p_{k-1} - \frac{p_{k-1}^2 x_k^2}{(1 + p_{k-1} x_k^2)} \quad (\text{D.5})$$

Appendix E

Further Extended: Yaw Moment Model

In Section 3.5, the model selected for aerodynamic yaw moment model $\hat{M}_{a,z}$ had limited number of terms which resulted in low estimation and validation fit results of the estimated model. Here, the fit of the net external yaw moment model \hat{M}_z is further improved by including a large number of predictors to the aerodynamic yaw moment model $\hat{M}_{a,z}$. The output model is selected based on the work of [31] and [36] which takes into consideration the complex aerodynamic interactions using higher order terms composed of the variables $u, v, w, V_r, \sum \Omega_i$, given by,

$$\begin{aligned} \hat{M}_{a,z} = & \hat{\theta}_{24} + \hat{\theta}_{25}u + \hat{\theta}_{26}v + \hat{\theta}_{27}u^3V_r + \hat{\theta}_{28}v^2V_r + \hat{\theta}_{29}u \sum \Omega_i + \hat{\theta}_{30}uvV_r \\ & + \hat{\theta}_{31}uv^2 + \hat{\theta}_{32}uv + \hat{\theta}_{33}v \sum \Omega_i + \hat{\theta}_{34}uw^2 + \hat{\theta}_{35}uvw^2 \end{aligned} \quad (\text{E.1})$$

The estimated value of the parameters in (E.1) is given in Table E.1. The estimation fit for the extended model is about 75.57% with the inclusion of 12 terms which also has the bias term.

| Model Predictor | Parameter ($\hat{\theta}$) | Estimated Value | Units |
|-------------------|------------------------------|-----------------------|--|
| uvw^2 | $\hat{\theta}_{35}$ | $2.58 \cdot 10^{-3}$ | Nm^{-3}s^4 |
| uw^2 | $\hat{\theta}_{34}$ | $-6.67 \cdot 10^{-3}$ | Nm^{-2}s^3 |
| $v \sum \Omega_i$ | $\hat{\theta}_{33}$ | $-1.45 \cdot 10^{-5}$ | $\text{Nrad}^{-1}\text{s}^2$ |
| uv | $\hat{\theta}_{32}$ | $2.28 \cdot 10^{-3}$ | Nm^{-1}s^2 |
| uvV_r | $\hat{\theta}_{30}$ | $-3.13 \cdot 10^{-8}$ | $\text{N}(\text{m}\cdot\text{rad}^2)^{-1}\text{s}^4$ |
| $u \sum \Omega_i$ | $\hat{\theta}_{29}$ | $-6.02 \cdot 10^{-6}$ | $\text{Nrad}^{-1}\text{s}^2$ |
| v^2V_r | $\hat{\theta}_{28}$ | $2.12 \cdot 10^{-8}$ | $\text{N}(\text{m}\cdot\text{rad}^2)^{-1}\text{s}^4$ |
| u^3V_r | $\hat{\theta}_{27}$ | $-3.82 \cdot 10^{-9}$ | $\text{N}(\text{m}\cdot\text{rad})^{-2}\text{s}^5$ |
| v | $\hat{\theta}_{26}$ | $2.17 \cdot 10^{-2}$ | Ns |
| u | $\hat{\theta}_{25}$ | $1.02 \cdot 10^{-2}$ | Ns |
| 1 | $\hat{\theta}_{24}$ | $-3.84 \cdot 10^{-4}$ | - |
| | NMSE fit | 75.57 % | |

Table E.1: Estimated parameters for further extended moment model $\hat{M}_{a,z}$.

The validation fit of the extended yaw moment model $\hat{M}_z = \hat{M}_{a,z} + \hat{M}_{hov,z}$ is given in Figure E.1.

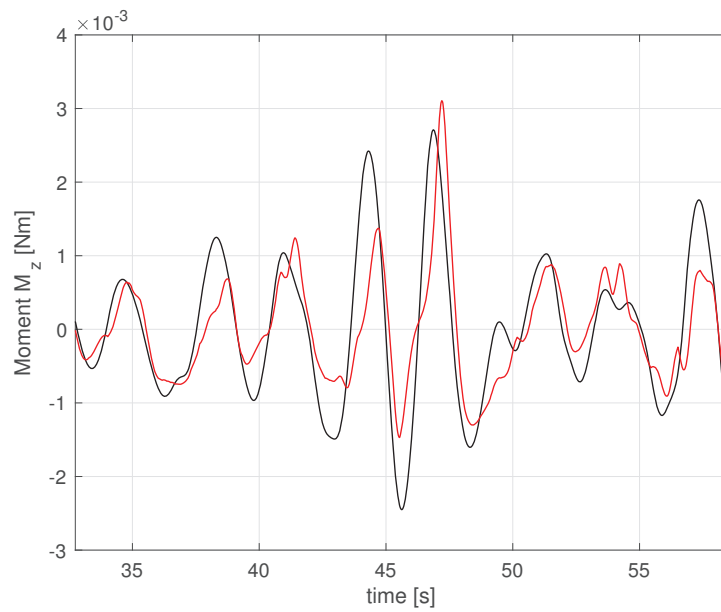


Figure E.1: Validation fit results on the measurement M_z (black) with identified extended yaw moment model \hat{M}_z (red) of NMSE fit 63.47 %.

Validation fit of 63.47% of the new moment model \hat{M}_z is lower than the estimation fit by about 12% which is expected since the number of terms have been increased significantly.